ΠΟΛΥΤΕΧΝΕΙΟ ΚΡΗΤΗΣ
ΣΧΟΛΗ ΜΗΧΑΝΙΚΩΝ ΠΑΡΑΓΩΓΗΣ & ΔΙΟΙΚΗΣΗΣ
ΕΡΓΑΣΤΗΡΙΟ ΜΙΚΡΟΚΟΠΗΣ & ΚΑΤΑΣΚΕΥΑΣΤΙΚΗΣ ΠΡΟΣΟΜΟΙΩΣΗΣ

Design of a contactless nonlinear energy sink for torsional vibration suppression

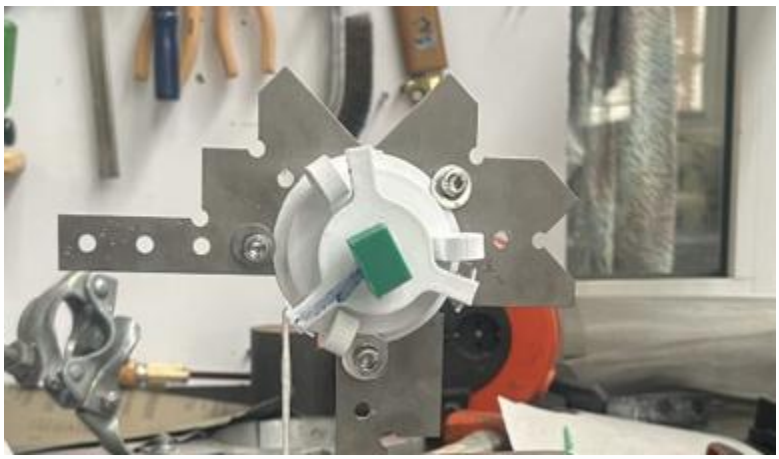

Mihai Ionut Trandafir

Εξεταστική Επιτροπή:

Αλευράς Παναγιώτης

Σταυρουλάκης Γεώργιος

Αντωνιάδης Αριστομένης

ΕΠΙΒΛΕΠΩΝ: Παναγιώτης Αλευράς

ΑΡ. ΔΙΠΛ.: 130

ΧΑΝΙΑ 2025

First of all, I would like to thank my supervisor, Dr. Panagiotis Alevras for his invaluable guidance and mentorship throughout my thesis journey. His exceptional expertise and unwavering patience have been instrumental in teaching me the intricacies of researching an unknown topic from scratch, and I am deeply grateful for the opportunity to have learned from him. Also, I would like to thank him for the valuable life lessons that he taught me almost on a daily basis. I would like to thank my family and my friends for being patient and supporting with me for this tough period of my life. Last but not least, I would like to thank the committee, the Technical University of Crete and the Micromachining & Manufacturing Modeling Lab (m3) for giving me the tools and opportunities to compile this thesis. Their support and resources have been essential in facilitating my research, and I appreciate the trust they have placed in me.

Contents

Abstract

Since an internal combustion engine provides torque only during one of the four phases of each piston’s movement, and due to the "Backlash" phenomenon, which arises as a result of the difference in the acceleration of the gears in a gearbox, torsional vibrations are generated at different frequencies that affect the vehicle and the driver. Traditional vibration absorbers are tuned to specific engine orders and thus are limited to narrowband attenuation. For this reason, a nonlinear energy sink (NES) will be designed to absorb these torsional vibrations. The nonlinearity of such a sink makes it ideal for this application as it has energy-dependent resonant response. To achieve this nonlinearity, magnets will be used. The reason magnets are used is the contactless nature of the applied magnetic torque and the flexible scaling of the required magnitude by manipulating the positions of the magnets and the intensity of the magnetic fields. Simulations of the restoring torque must be made, using Simcenter Magnet in order to find the right parameters for the NES. Then, using NX Siemens, the NES must be designed and be printed using additive manufacturing. Then, a static experiment must be done to compare the restoring torque of the manufactured NES compared to the one simulated. Last but not least, a dynamic experiment must be done to compare the manufactured NES’s dynamic properties to the simulated one.

1. Introduction

Due to the high demand of modernization and automation of industrial processes, mechanical systems are used in a wide range of applications, from automotive engines to industrial machinery. These systems are due to experience a constant or a fluctuating load of oscillations caused by the nature of their operation [1]. The frequency at which these oscillations occur may lead to resonance and high amplitude vibrations due to these frequencies being close to the natural frequency of the system [2].

Vibrations in mechanical systems can have catastrophic results such as fatigue, wear and failure of components. Torsional vibrations are particularly harmful in rotating machinery, as they can cause shafts to twist and break even if the torque applied is less than the theoretical maximum torque that the system can handle. In this thesis, we propose a novel design for a contactless nonlinear energy sink (NES) [3] that can suppress torsional vibrations in mechanical systems. The NES is based on the principle of nonlinear normal modes, which allows it to absorb and dissipate over a broad frequency range. The proposed concept utilizes magnetic interactions to realize the nonlinearity, benefiting from the absence of physical contact. This design has the potential to improve the reliability and performance of rotating machinery by reducing vibrations and increasing the lifespan of components due to the NES's ability to work on a bandwidth of frequencies.

In order to design the NES, we needed to find the optimal parameters of it. Since it would be cylindrical and contain cylindrical magnets perpendicular to the outer layer of it, the distance between the center of the magnets and the center of the NES needed to be found. Then we had to couple it with an adequate angle between the static magnets. Using Siemens' Simcenter Magnet software, we simulated the interaction between two static magnets and a moving magnet for R = 30, 45 and 60mm, each one with an angle of 60, 75, 90 and 120 degrees between the static magnets. Using MATLAB, we plotted each simulation and chose the one that fits better the equation describing the torque applied to it with linear and cubic stiffness. We opted for the one that had the largest cubic and smallest linear constant of the variables while at the same time, would have an acceptable R squared from the R squared analysis. Taking into consideration the conditions of the environment that the NES will work in, the type of magnets had to be decided. Due to the reliability and all the technical specifications the Neodymium Iron Born magnets have, we decided to move forward with N42 magnets since these magnets are more than enough for the needs of the thesis.

First, the reliability of the chosen magnets needed to be tested through an experiment. The experiment consisted of a static magnet connected to a load cell that was calculating the force applied to the magnet while the moving magnet was moving axially with respect to the static magnet. After comparing it with the simulation of the experiment that was done using Simcenter Magnet, the conclusion that the magnets should not come closer than 4 mm came. Based on this, the right configuration of R and θ was chosen.

The next step was to design and print the NES's components in 3D using the Raise3D Pro2 Plus printer that extruded PLA at about 205° C. After assembling the NES we calculated the Moment of Inertia of it, and using Tracker, an open source software, we saw it in action and we compared the Simcenter Magnet's simulated restoring torque and the printed NES's restoring torque using MATLAB.

Chapter 2 provides an insight of the theory that explains the means that were used to create the NES and what are the reasons for this creation. The way a traditional linear vibration absorber works along with how these vibrations occur, is thoroughly analyzed. Targeted energy transfer was also analyzed along with Hamiltonian systems and Frequency Energy Plots.

Chapter 3 dives deeper into the simulations and the process that occurred in order to define the parameters of the NES. The chapter then proceeds with the axial movement experiment of the magnets, in order to compare the applied force to the simulated one thus concluding the reliability of the magnets.

Chapter 4 describes the additive manufacturing process of creating the NES. Then, the NES was tested statically, in order to calculate the restoring torque, and dynamically, in order to compare the developed NES's ability to diminish the oscillations to the simulated values.

2. Literature Review

2.1 Vibration Absorbers

Vibration absorbers are devices that are used to reduce vibrations in mechanical and structural systems. They work by absorbing energy from the primary system and dissipating it with a local damper, thereby reducing the vibration amplitudes of the primary system. Vibration absorbers can be passive, semiactive [5] or active, depending on how they are controlled [4]. Passive vibration absorbers are typically tuned to the natural frequency of the system [6], while active vibration absorbers use sensors and actuators to control the absorber's response.

Vibration absorbers are commonly used in automotive engines, structures, industrial machinery and other rotating machinery to reduce vibrations and improve performance. Typical examples in automotive applications are Centrifugal Pendulum Dampers, which are tuned to suppress vibrations at a specific engine order.

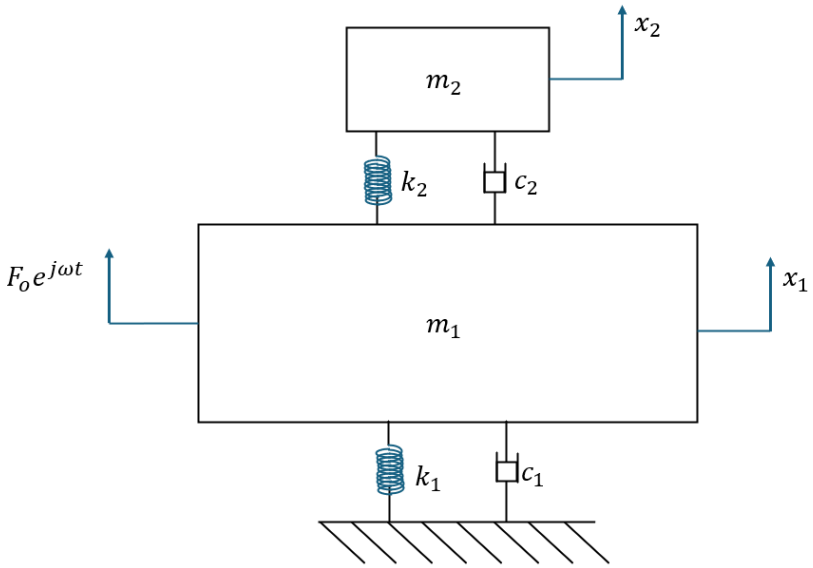

Figure 1 : Simple mass-spring-damper vibration absorber.

In *Figure 1* a sketch of the working principle of a linear vibration absorber is shown. The vibration absorber consists of a simple mass-spring mechanical system (m_2, k_2, c_2) that is attached to the vibrating system. The absorber is tuned to the natural frequency of the system, so that it resonates at the dominant vibration frequency of the primary system and absorbs energy from the system. From the general equation of motion of a single degree of freedom system, the equation of motion of the vibrating system can be written as:

$$M\ddot{x} + C\dot{x} + Kx = F(t) \qquad (1)$$

where M is the inertia matrix of the system, K is the stiffness matrix of the system, X is the displacement vector, and F(t) is the external force acting on the system. It should be noted that the external force can be due to the operation of the system, such as the torque generated by the engine in a rotating machinery. The equation of motion of the absorber and the system's mass can be written as:

$$\begin{bmatrix} m_1 & 0 \\ 0 & m_2 \end{bmatrix} \ddot{X} + \begin{bmatrix} c_1 + c_2 & -c_2 \\ -c_2 & c_2 \end{bmatrix} \dot{X} + \begin{bmatrix} k_1 + k_2 & -k_1 \\ -k_1 & k_2 \end{bmatrix} X = \begin{bmatrix} F_o sin(\omega t) \\ 0 \end{bmatrix} \quad (2)$$

Where $X = \begin{bmatrix} x_1 \\ x_2 \end{bmatrix}$ are the displacements of the masses.

The standard solution for *Eq. 2* is:

$$x(t) = Xsin\omega t = \begin{bmatrix} x_1 \\ x_2 \end{bmatrix} e^{(j\omega t)} \quad (3)$$

Therefore, substituting the standard solution into *Eq. 2*, the following equations for the system are:

$$x_1 = \frac{[(k_2 - m_2\omega^2) + c_2\omega j]Fo}{det(K - \omega^2 M + \omega jC)} \quad (4)$$

$$x_2 = \frac{(k_2 + c_2\omega j)Fo}{det(K - \omega^2 M + \omega jC)} \quad (5)$$

Where ω is the frequency of the vibrating system and $j = \sqrt{-1}$.

If the natural frequency of the absorber is equal or close to the natural frequency of the system, then the absorber will resonate with the system and absorb energy from it. In the theoretical undamped case, it's even possible to eliminate the primary system vibrations at a target frequency ω_T by withholding the tuning law, $k_2 = m_2\omega_T^2$. In practical applications with the presence of damping, this will reduce the amplitude of the vibrations in the system and improve its performance. However, vibration absorbers have some limitations. For example, they require physical contact with the vibrating system, which can lead to wear and tear of the components. In addition, vibration absorbers are typically tuned to a specific frequency, so they may not be effective in reducing vibrations at other frequencies. To overcome these limitations, we propose a novel design for a NES that can suppress torsional vibrations in mechanical systems because of its ability to work contactlessly and maintain resonant response over a band of frequencies.

2.2 Noise, Vibration and Harshness

2.2.1 Vibration of an electric motor

Industrialization came with the cost of global warming [7]. Since the first industrial revolution, fossil fuels have been continuously used to produce electrical and mechanical

energy with the downside of producing gases such as carbon dioxide, methane and nitrous oxides which lead to global warming that may cause long term effects, not only to humans but also to the flora of industrial heavy areas [8]. That's why most industries try to go on with a more environmentally friendly way of producing energy transitioning from internal combustion engines to electric engines. Even though electric engines in electric vehicles (EVs) are more efficient and reliable [9] than internal combustion engines (ICE), the broad torque response slope causes longitudinal vibrations due to driveline shock and torsion vibrations [10] [11] since the powertrain is directly coupled to its control grid and transmission system. The powertrain of an EV consists of the components responsible for generating and delivering power to wheels. These vibrations, when they are transferred to the seat of the driver, may cause a lot of physiological [12] problems. The problem with the absorption of these vibrations is that their natural frequency may not be stable. This means that using a linear energy absorber such as the one presented in the previous subchapter may not be very effective. That's why a NES that works with a bandwidth of frequencies, is more suitable for absorbing these vibrations.

2.2.2 Gear Rattle and torsional vibrations in ICEs

Torsional vibrations could be caused by gear rattling [13]. This is a phenomenon that occurs as backlash is caused when two gears have different accelerations, therefore the gears 'hit' each other. These impacts are transmitted to the housing through the transmission shaft and the bearings. The frequency of these impacts may vary depending on the shift in speed of each gear. Again, because the frequency is not constant, a NES could diminish the amplitude of these vibrations for a large scale of frequencies.

Some tortional vibrations could also be caused by the cycles and the phases of the cylinders that an ICE consists of. The cycle of a cylinder consists of four phases and only one of these phases produces torque that mobilizes the crankshaft.

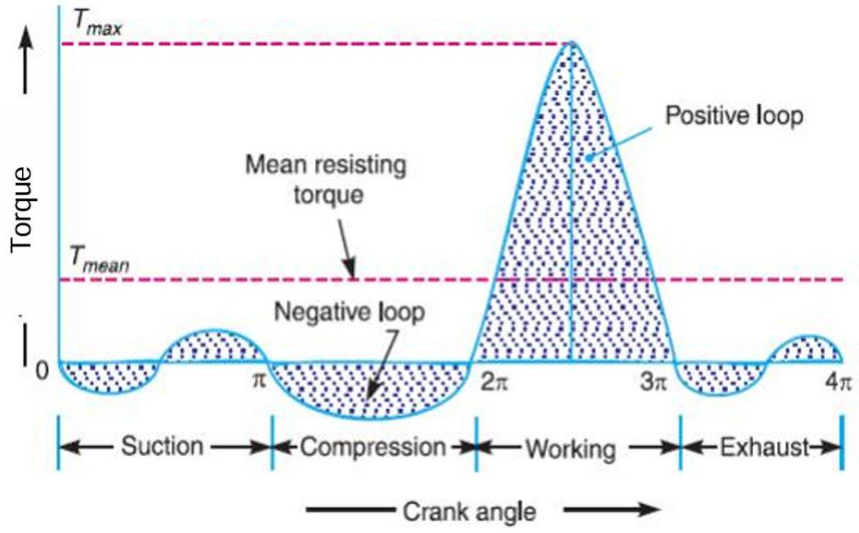

Figure 2 : Torque Diagram for a Four-Phase Engine with One Cylinder

This introduces periodic torsional vibrations in the powertrain as the crankshaft accelerates and decelerates. The number of cylinders plays an important role in reducing the frequency of the vibrations that the working phases may cause by adding more working regions per rotation. However, torsional vibrations may persist even when with many cylinders.

2.2.3 Noise, Vibration and Harshness

A good way of determining if these vibrations may be present and diminish the performance, the endurance of a system and the comfort of the user is through Noise, Vibration and Harshness (NVH) analysis. This analysis provides a way to determine if a particular section of the system is under high stress due to the vibrations. In a vehicle for example, the powertrain provides the greatest source of NVH emissions through the engine. At low rotations per minute (rpm) when the NVH emissions of the engine are the lowest and the vehicle is idling, being able to hear noise or feel vibrations from other components of the vehicle may induce a problem with that component or poor craftmanship [14].

2.3 Permanent Magnets

For the experimental trials of this thesis, specific magnets needed to be chosen. The magnets needed to be cost effective, have good magnetic strength and good thermal stability. The Neodymium Iron Born (NdFeB) magnets are a good choice. These magnets are used in all industries, from aerospace to food preparation, and are split into different groups based on their Max Energy Production (MEP), in Mega-Gauss-Oersteds (MGOe) units and their maximum operating temperature [15]. For example, Nxx (x is a number) magnets operate up to +80 degrees Celsius but NxxM , NxxH , NxxSh and NxxVH are rated from +100 degrees

Celsius to a maximum of +230 degrees Celsius [16]. In some cases, the maximum temperature that weakening of magnets occurs is slightly larger than the recommended maximum temperature [17]. For the experiments, the N42 magnets were chosen since the temperature of the experiments are close to room temperature and the 42 MGOe capabilities of the magnets are more than enough for the needs of this experiment.

Magnet Type	**BH_{max} (MGOe)**
Ferrite (Ceramic)	~3-5
Alnico	~5-9
Samarium Cobalt	~15-30
Neodymium (N35-N52)	~35-52

Table 1 : Different kinds of magnets and their BH_{max}

The Maximum Energy Product (BH_{max}) is a very important property of permanent magnets that represents the maximum amount of magnetic energy stored per unit volume. It determines the magnet's ability to store and deliver magnetic energy and a higher one means a stronger magnet per unit volume, which is useful when size constraints are rendering the use of larger magnets inappropriate. The N42 magnets provide a strong field while being cost effective, making them a good choice for the NES' design. Typical BH_{max} values are shown in *table 1*.

Before the 1950s, the manufacturers had to develop magnets in strange shapes in order to avoid self-demagnetization [44]. The 'hard magnet' (HM) is a magnet which has a broad hysteresis loop, which is a plot of the magnetization M of the material versus the magnetic field H acting on it. The loop is nonlinear, and it depends on time, temperature and the prior use of the magnet [45]. H_d is the demagnetizing field produced by the magnet itself which can be approximated by $H_d = -NM$, where $N \in (0,1)$ that depends only on the magnet's shape. H_o is the externally applied field and the total field acting is $H = H_o + H_d$. So, the magnetic field can be described by $B = \mu_o H$, where $\mu_o = 4\pi x 10^{-7} T\mu A^{-1}$ or $B = \mu_o(H + M)$ inside a magnetic material. A magnet inherently generates a demagnetizing field, because the magnetic field produced by the magnet opposes its own magnetization, and this phenomenon tends to depend on the geometry of the magnet. The longer and narrower magnets are in the direction

of magnetization, the higher the permeance coefficient tends to be, meaning they experience less internal demagnetization. The permeance coefficient is a parameter of the magnetic flux density inside the magnet (B_m) and the demagnetizing field at the operating point, as seen in *Eq. 6*.

$$Pc = B_m/H_d \qquad (6)$$

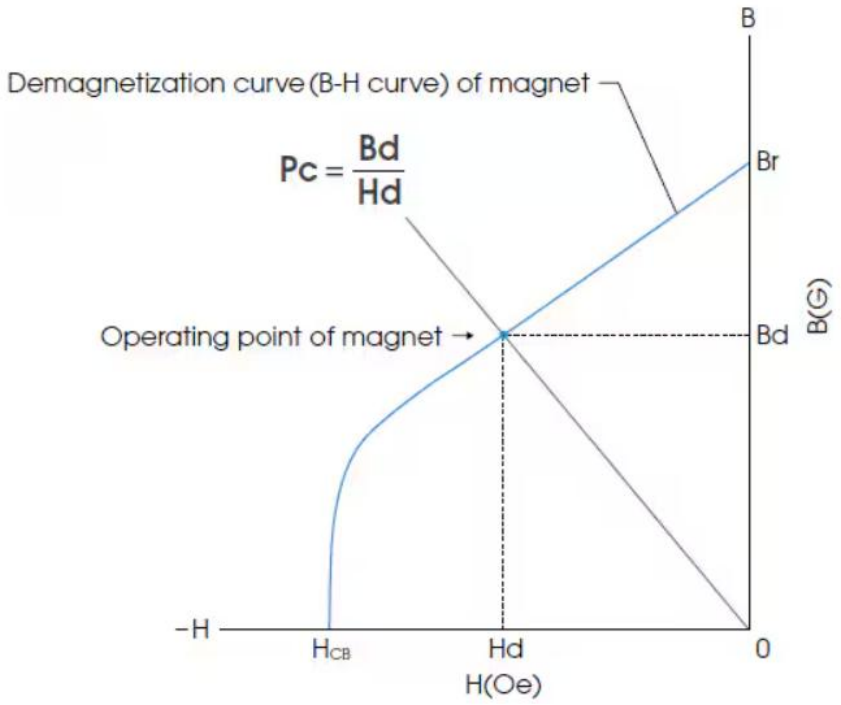

Figure 3 : Demagnetization curve of magnet and the Permeance coefficient.

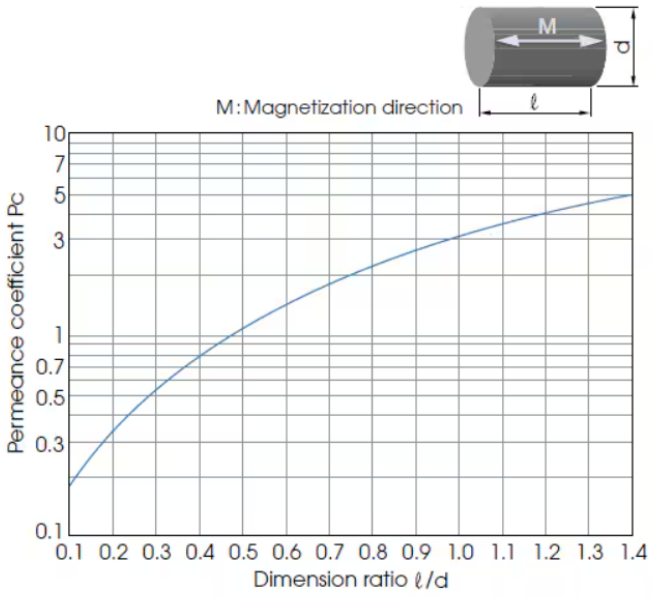

Figure 4 : Permeance coefficient for a cylindrical magnet.

For cylindrical shaped magnets, using *Eq. 7* we can calculate the magnetic flux density on any point 'x' on the central axis of the magnet for two opposing magnets.

$$B(x) = 2[\frac{Br}{2}(\frac{L + x}{\sqrt{R^2 + (L + x)^2}} - \frac{x}{\sqrt{R^2 + x^2}})] \qquad (7)$$

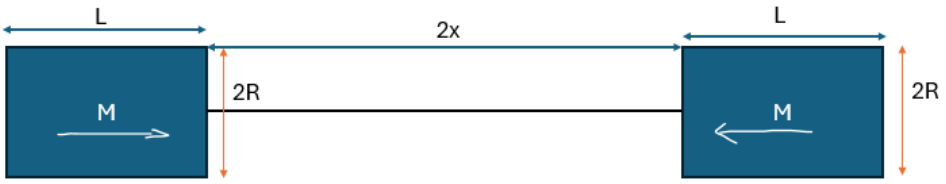

Figure 5 : Two magnets opposing each other.

Generally speaking, demagnetization can also occur from high temperatures or exposing magnets to opposing external fields. This effect occurs to permanent magnets that have a nonlinear demagnetization curve. These fields could either be created by current carrying conductors or by allowing magnets to come into contact with other magnets who have

opposing fields. Shock and vibrations have very little to no effect on demagnetization, but extremely high radiation could result in flux changes and demagnetization.

2.4 Targeted Energy Transfer (TET) & Hamiltonian Systems

Targeted energy transfers, where the energy is directed from a source (donor) to a receiver (recipient) in a one-way irreversible fashion, take place in many applications. Alexander F. Vakakis [18] implied that passive TET from the directly excited linear oscillator to the NES is realized when the energy exceeds a certain critical threshold. The mathematical description of the TET process is complex due to its transient, and not steady, state and due to being essentially nonlinear instead of weakly nonlinear. It should be noted that the efficiency of TET depends on parameters like the nonlinearity strength, damping characteristics and mass ratio between the primary system and the NES [38].

Before getting into TET, a discussion of Hamiltonian systems needs to be held [39]. First of all, a Hamiltonian system is a dynamic system that is ruled by Hamilton's equations. This system may describe the evolution of a physical system such as a planetary system or an electron in an electromagnetic field. The advantage of this approach is that it gives important insights into the dynamics even if the initial value problem cannot be solved analytically. The system can be characterized by the scalar function $\boldsymbol{H}(\boldsymbol{q},\boldsymbol{p},\boldsymbol{t})$ and the state of the system $\boldsymbol{r}$ is described by the generalized momentum and position, $\boldsymbol{p}\ and\ \boldsymbol{q}$. It should be noted that $p,q \in R^N$ and that the state of the system can be completely described by $r \in R^{2N}$ with $r = (q,p)$. Thus, the evolution equations are given by Hamilton's equations as: $\mathrm{dp/dt} = -\vartheta H/\vartheta q\ and\ dq/dt = \vartheta H/\vartheta p$. If the Hamiltonian is not explicitly time-dependent then the Hamiltonian does not vary with time at all and so, the Hamiltonian is a constant of motion whose constant equals the total energy of the system $H = E$.

Examples of such systems are the undamped pendulum and the harmonic oscillator. So, the Hamiltonian equation for an undamped pendulum with a single degree of freedom is:

$$H = \frac{p^2}{2m} + \frac{kq^2}{2} with\ p = m\dot{x}\ and\ q = x \qquad (8)$$

And the evolution of the dynamical system can be generally written as:

$$\nabla_r H = \begin{bmatrix} \frac{\vartheta H}{\vartheta q} \\ \frac{\vartheta H}{\vartheta p} \end{bmatrix} \qquad (9)$$

$$\frac{dr}{dt} = M_N \nabla_r H(r) \; with \; M_N = \begin{bmatrix} 0 & I_N \\ -I_N & 0 \end{bmatrix} \; , where \; I_N \; is \; the \; identity \; matrix. \qquad (10)$$

Some studies have shown that TET can be achieved with ungrounded NESs possessing significantly smaller mass but with essentially nonlinear coupling to the primary system [41]. This implies that with the addition of lightweight, strongly nonlinear, local attachments one could gain the capacity to alter drastically the global dynamics of the primary system. In essence, the NES acts as a passive, self-adaptive boundary vibration controller because its nonlinearity provides an energy-dependent TET that dissipates passively adaptive dynamics that are fully tunable with energy.

As an example, let's consider a primary linear oscillator (LO) attached to a lightweight NES described by the following equations:

$$\begin{aligned} &\ddot{x} + \lambda_1 \dot{x} + \lambda_2(\dot{x} - \dot{y}) + \omega_o^2 x + C(x - y)^3 = 0 \qquad (11) \\ &\varepsilon \ddot{y} + \lambda_2(\dot{y} - \dot{x}) + C(y - x)^3 = 0 \end{aligned}$$

Where the first equation describes the movement of the LO and the second one describes the movement of the NES. Where x is the displacement of the LO and y is the displacement of the NES, the system is viscously damped and $0 < \varepsilon << 1$ is the mass ratio. Introducing the following complex variables:

$$\begin{aligned} &\psi_1(t) = (\dot{x(t)}) + jx(t) = \varphi_1(t) e^{(j\omega_o t)} \qquad (12) \\ &\psi_2(t) = \left(\dot{y(t)}\right) + jy(t) = \varphi_2(t) e^{(j\omega t)} \end{aligned}$$

Where φ_1 and φ_2 are slowly varying [40] complex modulations of the fast components with fast frequencies ω_o and ω. Since TET corresponds to 1:1 transient resonance capture (TRC) between the primary linear oscillator and the NES, we assume that the transient dynamics has only a single dominant fast frequency [41] then: $\omega \approx \omega_o = 1$. Thus, the equations can be written as:

$$\begin{aligned} &\psi_1(t) = \varphi_1(t) e^{(jt)} \qquad (13) \\ &\psi_2(t) = \varphi_2(t) e^{(jt)} \end{aligned}$$

If we assume that $\lambda_1 = \lambda_2 = \lambda$ for simplicity and express the complex variables in a polar form $\varphi_i = a_i(t) e^{(jb_i(t))}$, i = 1,2 since we have two equations, then a slow flow equation [40] is formed expressed in terms of real variables:

$$\dot{\alpha_1} - (\varepsilon\lambda/2)\alpha_2 cos\varphi + \varepsilon\lambda\alpha_1 + (3C/8)(\alpha_1^2 + \alpha_2^2 - 2\alpha_1\alpha_2 cos\varphi)\alpha_2 sin\varphi = 0 \qquad (14)$$

$$\dot{\alpha_2} + (\lambda/2)\alpha_2 - (\lambda/2)\alpha_1 cos\varphi - (3C/8\varepsilon)(\alpha_1^2 + \alpha_2^2 - 2\alpha_1\alpha_2 cos\varphi)\alpha_1 sin\varphi = 0$$

$$\dot{\varphi} + (\lambda/2)[(\varepsilon\alpha_2/\alpha_1) + (\alpha_1/\alpha_2)]sin\varphi - 1/2$$

$$+ (3C/8)(\alpha_1^2 + \alpha_2^2 - 2\alpha_1\alpha_2 cos\varphi)\left[(1/\varepsilon)[1 - (\alpha_2/\alpha_1)cos\varphi] - [1 - (\alpha_1/\alpha_2)cos\varphi]\right]$$

$$= 0$$

Where $\alpha_1 \, and \, \alpha_2$ represent the real amplitudes of the slowly varying of the linear and nonlinear responses, respectively and $\varphi(t) = b_1(t) - b_2(t)$ is the slow phase difference between the evolution of the two envelopes. The graph of the *Eq. 11* for $\varepsilon = 0.05, \lambda = 0.01, C = 1, \omega = 1$ and initial conditions $\alpha_1(0) = 0.24, \alpha_2(0) = 0.01 \, and \, \varphi(0) = 0$ is illustrated in *Figure 6.*

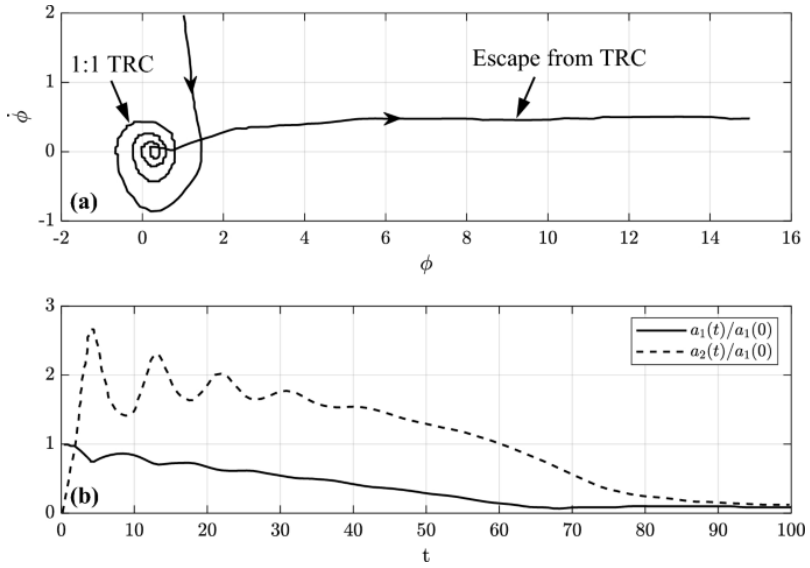

Figure 6 : Dynamics of fundamental (1:1 Resonance) TRC a) Representation of the $(\varphi, \dot{\varphi}) \, plane$ and b) the evolution of the normalized amplitude modulations of the linear oscillation and the NES. [18]

In the *Figure 6*, the TRC (1:1) is confirmed since it suggests that the NES and the LO, for the neighborhood of φ = 0, are in phase. In that area, energy is transferred from the primary LO system to the NES as shown in the lower figure. For more complex mDOF systems, it was proven that mainly Hamiltonian systems (undamped and unforced) are responsible for the greater part of the TET [41] in the dissipating system.

In the absence of damping and external forces, *Eq. 11* turns into:

$$\ddot{x} + \omega_o^2 x + C(x - y)^3 = 0 \qquad (15)$$

$$\varepsilon\ddot{y} + C(y - x)^3 = 0$$

A more suitable representation of the computed NNMs is to depict their frequency indices (FIs) as functions of their energies h in a FEP. For $C = 1, \omega_o = 1 \; and \; \varepsilon = 0.05$, in ***Figure 7***, an NNM branch represented by a solid line, is a collection of periodic orbits possessing the same qualitative features. Bifurcation points are also indicated in this plot with (+) and (o) used to indicate changes of stability. If the NES didn't have a cubic stiffness, the figure would consist merely of two vertical lines at the frequency of the primary system and the absorber. The figure is better explained by the book "Nonlinear Targeted energy Transfer in Mechanical and Structural Systems" by Valakis, Gendelman, Bergman, McFarland Kerschen and Sup Lee [18].

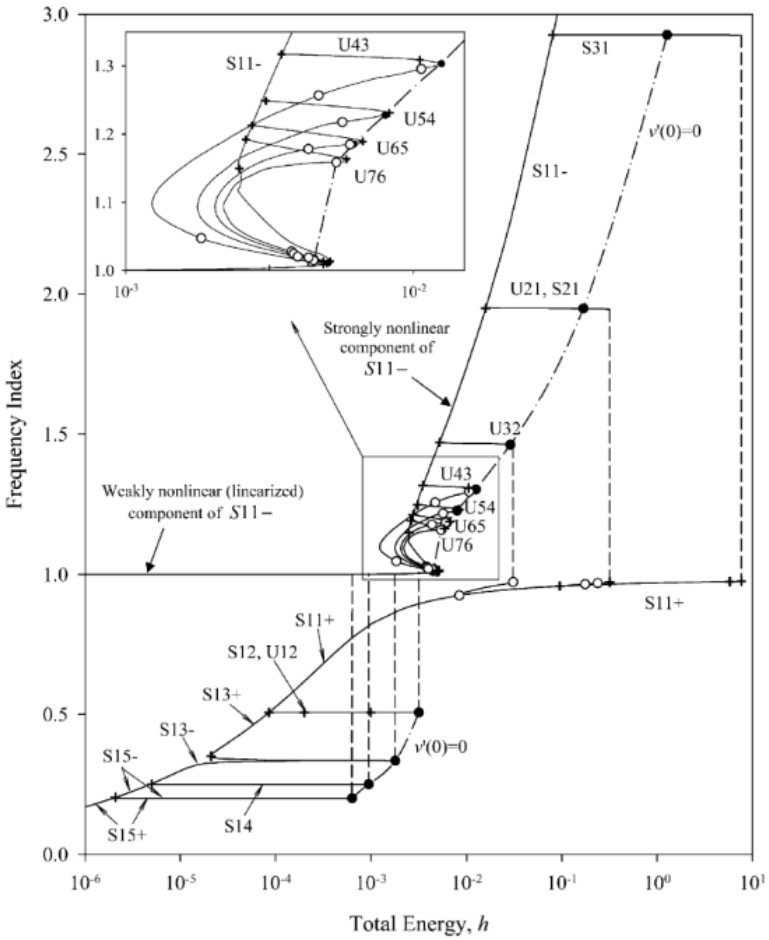

Figure 7 : FEP of NES that is described in Eq. 20.

2.5 Nonlinear Energy Sink (NES)

The main goal of vibration absorbers is to protect dynamical systems from destructive vibrations by passively transferring and dissipating the unwanted energy. The reason why an NES would be suitable for the design of a vibration absorber is because it also has a non-linear

stiffness apart from the linear stiffness. If we consider a non-linear absorber that has both a linear and a nonlinear stiffness, then, modifying *Eq. 2* the equation of motion of the absorber would be:

$$m_2\ddot{x_2} + c_2(\dot{x_2} - \dot{x_1}) + k_{2,L}(x_2 - x_1) + k_{2,NL}(x_2 - x_1)^3 = 0 \qquad (16)$$

Where $k_{2,L}$is the coefficient of linear stiffness and $k_{2,NL}$is the coefficient of non-linear stiffness. The operation of an NES can be explained by looking at how it absorbs energy and how it redistributes and dissipates it [18] [19]. Due to the redistribution of energy within the modal space of a vibrating system, the nonlinear behavior scatters the vibration energy from lower frequency modes into higher frequency modes. The key difference between linear and nonlinear systems is that the linear system's mode frequencies are constant regardless of energy input and that the nonlinear system's mode frequencies increase with energy input as shown in *Eq. 17*.

$$\omega_{NES} = \sqrt{\frac{k_{2,L}}{m_2} + \frac{3k_{2,NL}A^2}{8m_2}} \qquad (17)$$

The process of transferring energy from a dynamical system to another dynamical system irreversibly is called targeted energy transfer (TET) [20]. This process comes from the nonlinear coupling of the NES with the dynamical system [21]. If the NES employed purely cubic stiffness without a linear part, it would enable the NES to be engaged in multiple resonance captures [40].

The frequency energy plots (FEPs) [42] analysis plays an important role in revealing the nonlinear dynamical signature of the NES. Basically, the FEPs are graphical representations that show how the system's natural frequencies change as a function of energy. These plots are particularly useful in nonlinear dynamics to understand how energy influences system behavior, especially when nonlinearities cause frequency shifts. The key features of FEPs [42] are:

- X-axis: Represents the system's total energy.
- Y-axis: Represents the system's natural frequencies or mode frequencies.
- Nonlinear Effects: In linear systems, frequency remains constant regardless of energy. In nonlinear systems, frequency can change with energy due to effects like stiffness softening or hardening.
- Bifurcations & Modal Interactions: FEPs help identify points where nonlinear modal interactions, bifurcations or internal resonances occur.

- Application to NES: FEPs can help analyze how energy levels affect the nonlinear damping characteristics of the NES.

The periodic motion of NES systems has been extensively studied on the harmonic backbone curves of nonlinear normal modes (NNMs) and their associated branches of subharmonic and super harmonic periodic motions in the FEPs [40] [41]. The resonance captures in the FEPs have explained the passive energy absorption and dissipation which is achieved by the nonlinear action of the NES.

The way an efficient TET process by a NES attachment operate should include:

- The energy that is being transferred to the NES should be one-way. This means that the least amount of energy should be able to transfer back to the dynamical system.
- Fast absorption and dissipation of significant energy from the primary system.
- The energy transfer should occur over a wide range of frequencies [22].
- The efficiency of the TET should not be mitigated by changes in the dynamical system's parameters.

The NES's history is quite interesting. Everything started when nonlinear energy sinks were mere linear systems coupled together [23]. The nonlinearity was formed by elastic elements [24], wire ropes [25] and beams and magnets [26]. For example, nonlinear stiffness has been created with the help of two oblique springs as shown in the following figure [27].

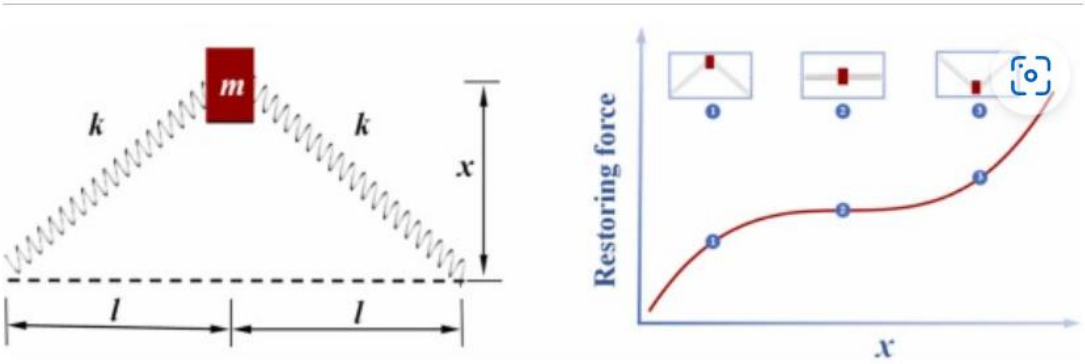

Figure 8 : Nonlinearity created with two springs [28].

In another study, conical springs were used to create a cubic stiffness [43]. In that study, a NES was used in a small-scale propulsion rig. The two main inertias of the propulsion system are excited by the cyclic irregularities originating from an engine or motor. The experiment was a success and depicted significant vibration attenuation in the frequency range 55-70 Hz.

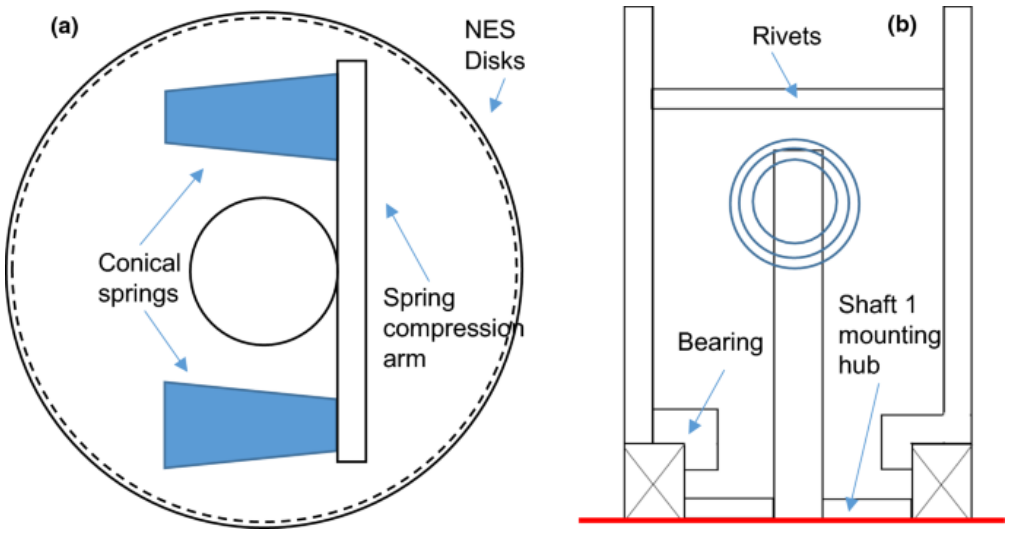

Figure 9 : The NES that was created using conical springs [43].

Designing nonlinear vibration absorbers is quite challenging due to the inherent complexity of nonlinear dynamics. Unlike their linear counterparts, these absorbers exhibit amplitude-dependent stiffness and damping, leading to phenomena such as bifurcations, multiple stable and unstable responses, and extreme sensitivity to even small parameter variations. Moreover, ensuring the necessary physical contact between the nonlinear spring elements is critical. In many designs, strong physical interaction is needed to trigger the desired nonlinear response. This often involves managing involves managing complex contact phenomena like (friction, impacts, etc.), where even small deviation in contact conditions can dramatically impact the absorber's effectiveness. For example, the fine tuning of the above-mentioned NES, resulted in the experimental success of diminishing the vibration of the propulsion system for the broad range of frequencies.

3. NES Design

3.1 Reliability of the N42 Magnets

3.1.1 Theoretical Procedure

For this thesis, the initial step was to experiment with the magnets and find out the reliability of the theoretical-simulated data by comparing it with in-house produced relevant experimental data of the magnetic force. Using Simcenter Magnet 2022.1 [30], a software developed by Siemens, a simulation of linear movement between a static magnet and a moving magnet was done. The magnets were constantly in repulsion [29] and the repulsive magnetic force was measured. For this simulation, after trying out different maximum finite element meshing of the magnets and the boundary condition, the best maximum element size was found to be 0.5 mm for the magnets and 5 mm for the boundary condition, which in the

simulations that were made for the thesis, was air. The purpose of this simulation was to compare the computational results with experimental data in order to establish the reliability of the computational models.

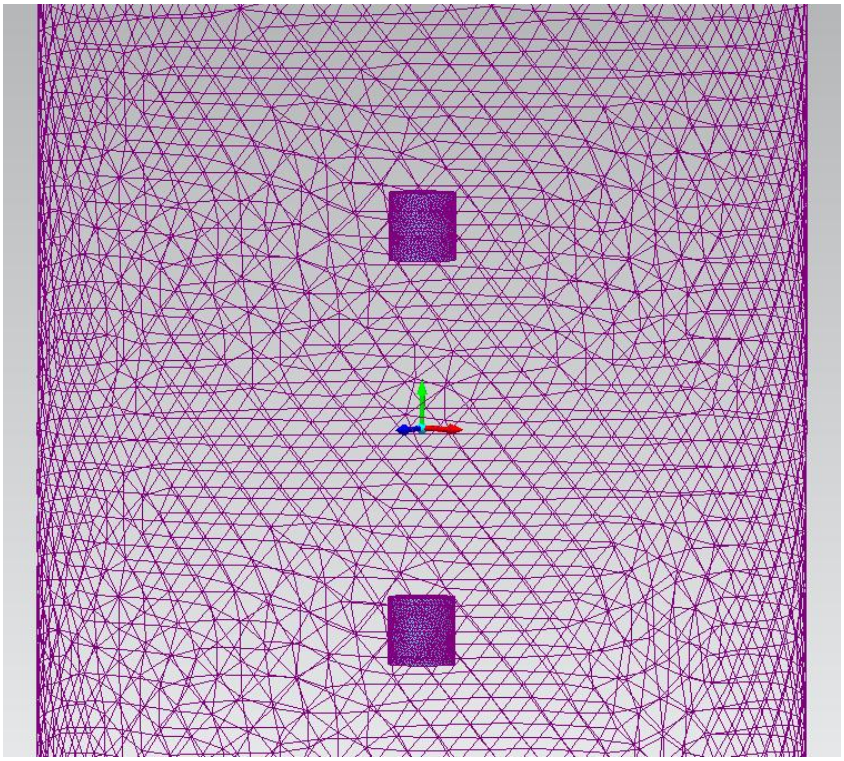

Figure 10 : Meshing of the linear movement experiment for the N42 magnets and the air.

The magnets for the NES are cylindrical N42 permanent magnets with an upper and lower radius of 4mm and a height of 8mm. The geometrical choice for the magnets was due to their optimal balance between magnetic strength, size and feasibility for precise measurements [31]. The chosen dimensions offer a practical compromise between magnetic force and spatial constraints, allowing for controlled interactions between the magnets while ensuring their alignment and movement remain consistent throughout the experiments. The settings for the transient simulation were polynomial order 2, with max. Newton iteration 50 and with a tolerance of 1%. These settings reassured us that the solution would be as accurate as possible. Also, the boundary condition should be 6-7 times wider than the diameters of the magnets in order to let the magnetic flux flow as it needs.

3.1.2 Experimental Procedure

For the experiment, an electronic vertical ruler, a max 5kg Load Cell, an Arduino R3 with digital and analog inputs/outputs and a HX711 amplifier were used.

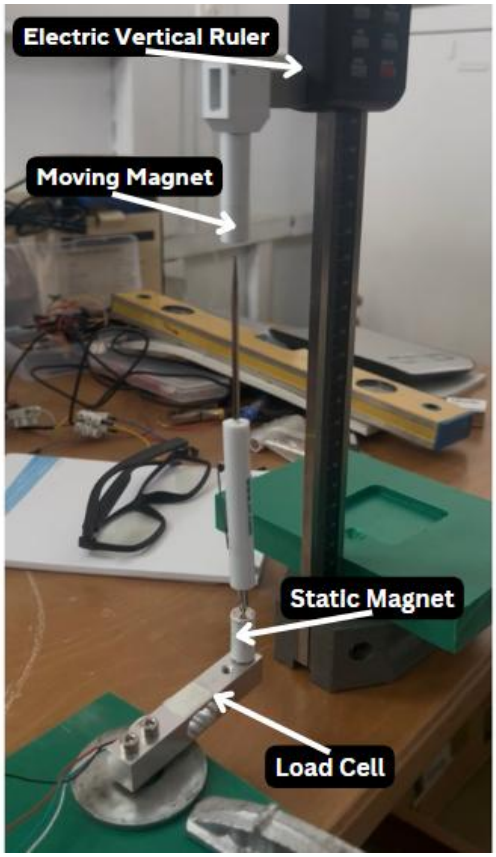

Figure 11 : The static Magnet, the moving magnet, the load cell and the electronic vertical ruler for the experiment.

An Arduino script [33] (*Appendix A*) was written in order to read the data from the load cell. At the beginning of the script, the moving magnet was moved far from the static magnet and the taring of the load cell occurred. Then slowly the moving magnet was transferred closer to the static magnet and the distance from the static magnet and the force it was applying to it was recorded. It should be noted that for the housing of the magnets, Siemen's NX was used to design them and Prusa's PrusaSlicer was used to create the 3D printing G-Code [34], using Polylactic Acid (PLA) [35]. The 3D Printer that was used to print the components was the Raise3D Pro2 Plus and the print took 3 hours, it used 7.7 grams of the PLA which is about 2.6 meters. The nuzzle that extruded the PLA was at a constant 205°C and the printer's bed was at about 75°C. It should be noted that the highest possible settings were used in order to have the accuracy needed for the experiment. A metallic screwdriver was placed in order to calibrate the two magnets and make sure that they are aligned.

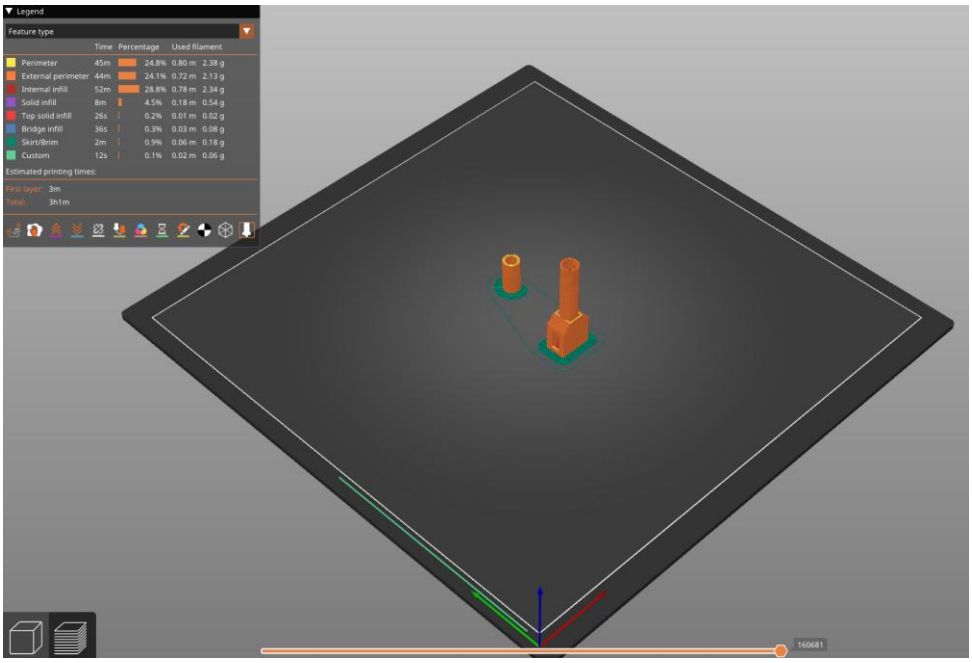

Figure 12 : PrusaSlicer's interface for printing the components for the linear movement of the magnets.

Load cells are very reliable tools to use for measuring force and torque. The way that these components measure force is through displacement using strain gauges as the sensing element [32]. The strain gauges are placed in a Wheatstone bridge circuit in order to measure resistance change in them.

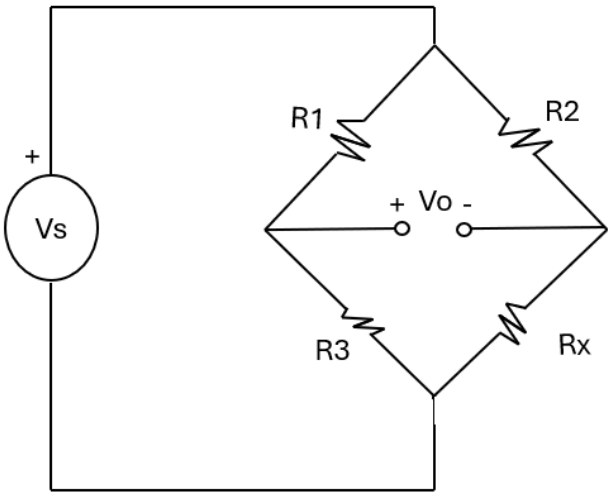

Figure 13 : Wheatstone bridge circuit.

Supposedly, if all the resistors have the same value, when there is a change in resistance then the R_x resistance is given by the following equation.

$$R_x = R\left(1 + \frac{\Delta R}{R}\right) \qquad (18)$$

Where ΔR/R is the fractional change in gauge resistance because of strain.

When ΔR/R > 0 , then the off-null voltage is given by [32]:

$$V_o = -\frac{V_s}{4}\frac{\frac{\Delta R}{R}}{1 + \frac{\Delta R}{2R}} \qquad (19)$$

And the force that is applied to the load cell is calculated through the following equation.

$$F = V_o * 4\frac{AE}{G_f V_s} \qquad (20)$$

Where: V_o is given by *Eq. 19*, A is the area of the load cell at the strain gauge location where the force is applied to, E is the Young's module of the material and G_f is the gauge factor of the strain gauge. It should be noted that it is typically around 2 for metal strain gauges.

3.1.3 Conclusion

According to the recorded data, it was concluded that only after 4mm the simulation's data and the experiment's data match. The reason for this could be the accuracy of Simcenter Magnet's model that it uses to simulate the experiments or the way we proceeded to do the experiment. The load cell's data could have been invalidated by environmental noise or the vertical ruler's magnet holder could have misaligned due to the great forces that occur closer to the magnet. Taking this into consideration, the magnets should not come closer than 4mm in the forthcoming experiments and in the NES's design.

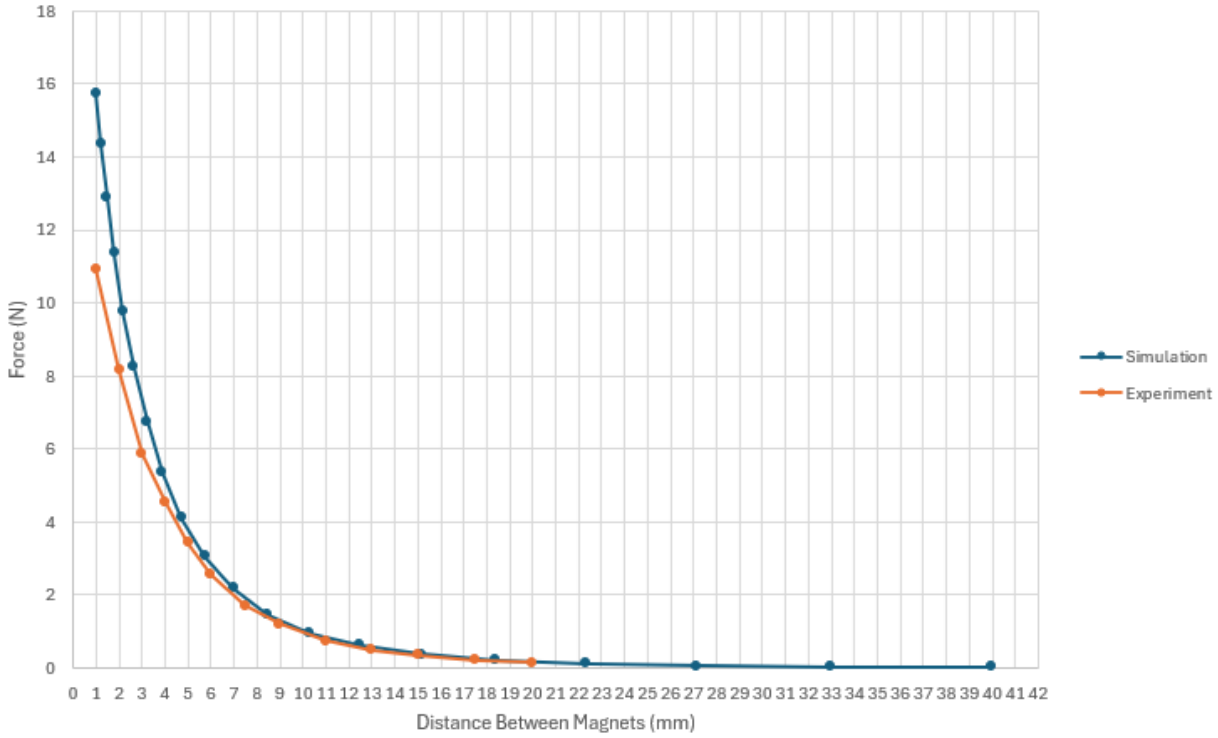

Figure 14 : Comparing the data from the simulation and the experiment for the vertical movement of the magnets.

3.2 Rotary movement of the magnets

3.2.1 Theoretical Procedure

Using Simcenter Magnet, we designed and simulated the interaction between two static magnets and a moving magnet. There was an angle θ between the center of the two static magnets and a moving magnet that had dynamic orientation based on the angle φ between it and the lower static magnet. The magnets were displaced at a distance R from the center of the axis. For each $R = 30, 45 \; and \; 60 \; mm$ a $\theta = 60°, 75°, 90° \; and \; 120°$ simulation was created.

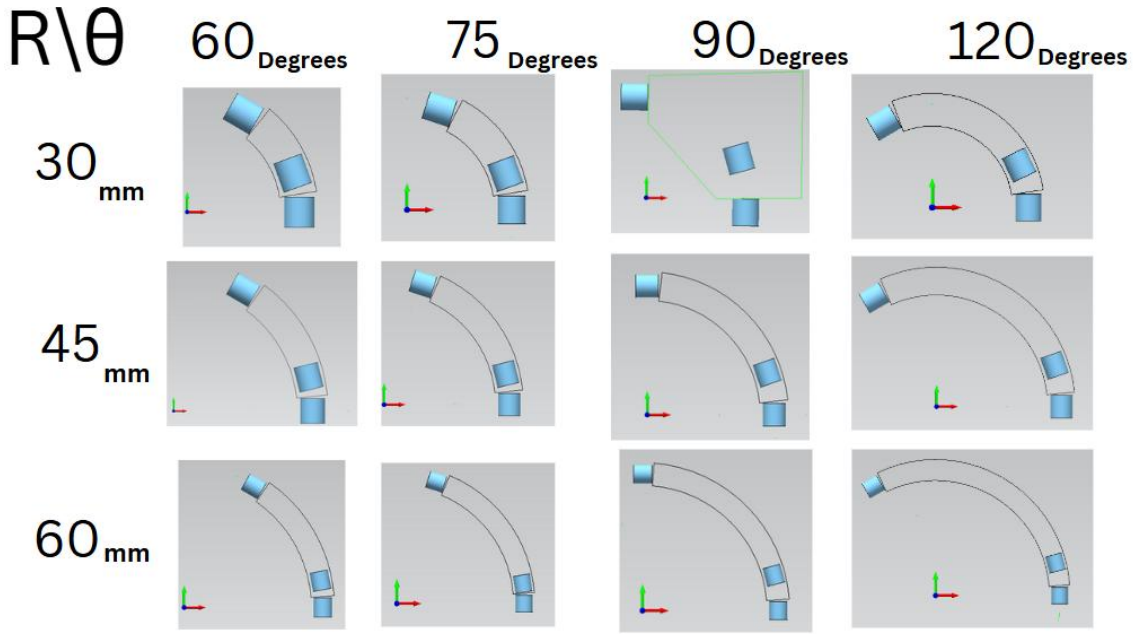

Figure 15 : Designs of all the rotary simulations of two static magnets and a rotating magnet.

Since it was concluded in chapter 3.1.3 that the experimental data corresponds to the simulated data only for a distance greater than 4mm, all the 60° and 75° simulations became obsolete. The reason is:

$$R\theta - 4 \geq l = R\varphi \geq 4\,mm$$

$$l_1 = \left(R - \frac{d_m}{2}\right)\varphi \geq 4\,, \varphi \geq \frac{4}{R - \frac{d_m}{2}}(rad)\ and\ l_2 = \left(R + \frac{d_m}{2}\right)\varphi \leq (R\theta - 4) \qquad (21)$$

Where the $d_m$is the diameter of the magnets and φ is the angle between the moving magnet and the lower static magnet. The same must be true between the upper static magnet and the moving magnet taking into consideration the height of the magnet. Basically, *Eq. 21* shows the upper and lower bound that the magnet can move. If the range of φ is too small, then the testing is unreliable and should not occur. So, this concludes that the simulations that had a θ of 60 or 75 degrees had an extremely small range for φ, in order for it to be taken into account on deciding the design of the NES.

The restoring torque of each simulation can be seen in the following tables (*table 2.1, table 2.2 & table 2.3)*.

R30 Theta 90		R30 Theta 120	
θ (degrees)	Torque (Nm)	θ (degrees)	Torque (Nm)
16	0.040652373	7.7	0.099606966
20.8	0.023138916	14.43	0.038587922
25.6	0.012949669	21.16	0.017285906
30.4	0.006388112	27.89	0.008141747
35.2	-0.00519837	34.62	0.003399732
40	-0.00456743	41.35	0.000105859
44.8	-0.00553987	48.08	-0.00278709
49.6	-0.01394188	54.81	-0.00706935
54.4	-0.01811461	61.54	-0.01493443
58.24	-0.03875623	68.27	-0.03287651
		75	-0.08163876

Table 2.1 : Simulated Data for R = 30mm.

R45 Theta 90		R45 Theta 120	
θ (degrees)	Torque (Nm)	θ (degrees)	Torque (Nm)
7.1	0.096198997	7.2	0.094410413
12.09	0.037114358	14.36364	0.023072296
17.08	0.016643898	21.52727	0.007779066
22.07	0.007849704	28.69091	0.003203071
27.06	0.003410953	35.85455	0.001237285
32.05	0.00040378	43.01818	-5.93E-05
37.04	-0.00232373	50.18182	-0.000877534
42.03	-0.0058936	57.34545	-0.002423516
47.02	-0.01246198	64.50909	-0.00555075
52.01	-0.0269564	71.67273	-0.015438005
		78.83636	-0.054579581

Table 2.2 : Simulated Data for R = 45mm.

R60 Theta 90		R60 Theta 120	

θ (degrees)	Torque (Nm)	θ (degrees)	Torque (Nm)
6	0.106922521	6	0.107121158
12	0.027119422	10.4	0.037515762
18	0.009436146	14.8	0.01629197
24	0.003876767	19.2	0.007740444
30	0.0012805	23.6	0.004159313
36	8.00E-05	28	2.30E-03
42	-0.00113324	32.4	0.001382841
48	-0.00392456	36.8	0.000887324
54	-0.0092807	41.2	0.000554082
60	-0.02703516	45.6	0.000101274
		50	-3.94E-05
		54.4	-4.69E-05
		58.8	-0.000436519
		63.2	-0.000588566
		67.6	-0.001118529
		72	-0.001856962
		76.4	-0.003195251
		80.8	-0.005449188
		85.2	-0.011299368
		89.6	-0.0251665
		94	-0.064408931
		95	-0.1

Table 2.3 : Simulated Data for R = 60mm

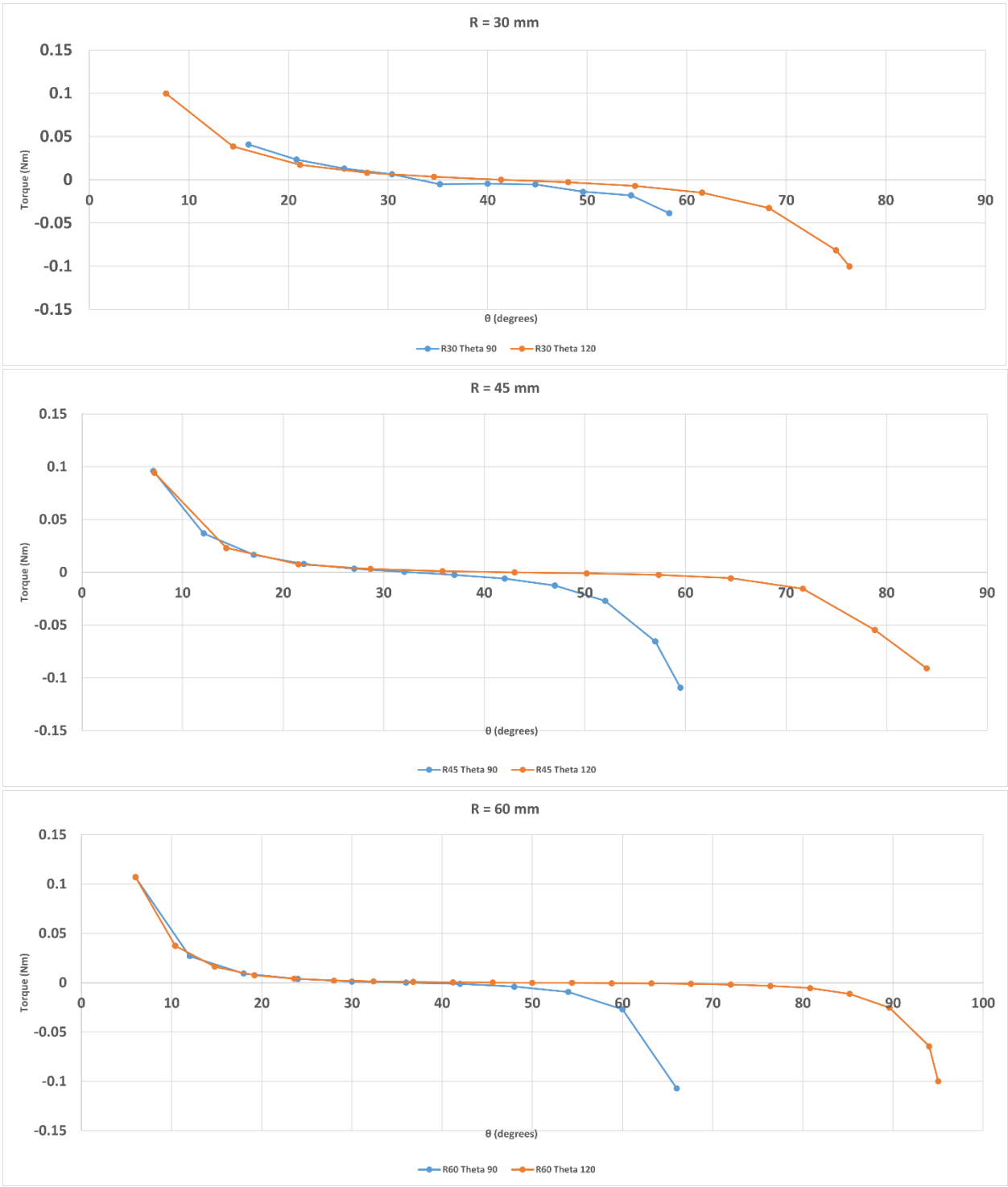

Figure 16 : Graph of the simulated restoring torque data.

For the chosen trajectory of the moving magnet, it can be noted that the maximum and minimum torque that it produces is around ±0.1 Nm except for the R=30mm θ = 90° which produces 0.035 Nm.

3.2.2 Post Processing of the simulated data

Using MATLAB's Curve Fitter App [36], the data was fitted in a 3rd degree polynomial equation, with the 2nd degree variable and the constant to be equal to 0. The reason is that the equation that would give the restoring torque produced by the moving magnet, needed to an equation with a linear and a 3rd degree variable in the form of *Eq. 22*. The results are as shown in *table 3*.

$$T(\theta) = a\theta^3 + b\theta \qquad (22)$$

θ is the angle between the lower static magnet and the moving magnet, *a* and *b* are constants from the fitting.

R/θ	R30 θ90	R30 θ120	R45 θ90	R45 θ120	R60 θ90	R60 θ120
a	0.518	0.4339	0.9954	0.2741	0.6493	0.1486
b	0.0342	0.001	0.0001	0.001	0.001	0.001
a*θmax	0.1909	0.2599	0.4552	0.1837	0.34	0.1154
b*θmax	0.0126	5.99e-04	4.572e-0.5	6.7021e-04	5.236e-04	7.7667e-04

Table 3 : Fitted data showing a and b for Eq. 22.

Taking into consideration *Eq. 23* for all simulations, this means that mostly nonlinearity contributes to the creation of the restoring torque. This can be concluded from *Eq. 23.* This equation shows that the nonlinear part of *Eq. 22* plays a greater role in the torque that is created than the linear part.

$$\int (|a|\theta^3 - |b|\theta)d\theta > 0 \qquad (23)$$

Doing an R squared [37] analysis of each fit, we conclude that the fitting of R = 30mm θ = 120° is the most reliable with an R squared of 0.9895.

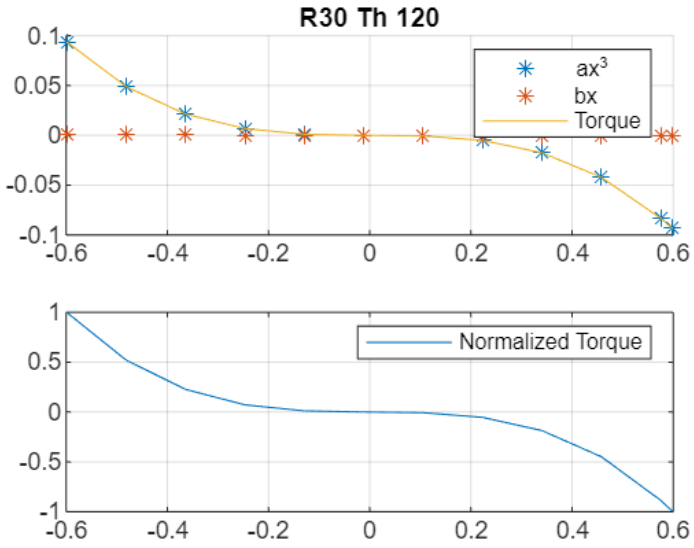

Figure 17 : plot of R30θ120 torque (y-axis) and each attribute of the it (upper Figure) and the Normalized torque (lower Figure) with the x-axis as rads.

After choosing the parameters R and θ (angle between the two static magnets), a simulation of the three-axis contactless NES has been created to make sure that the alignments and the torque of the magnets are constant.

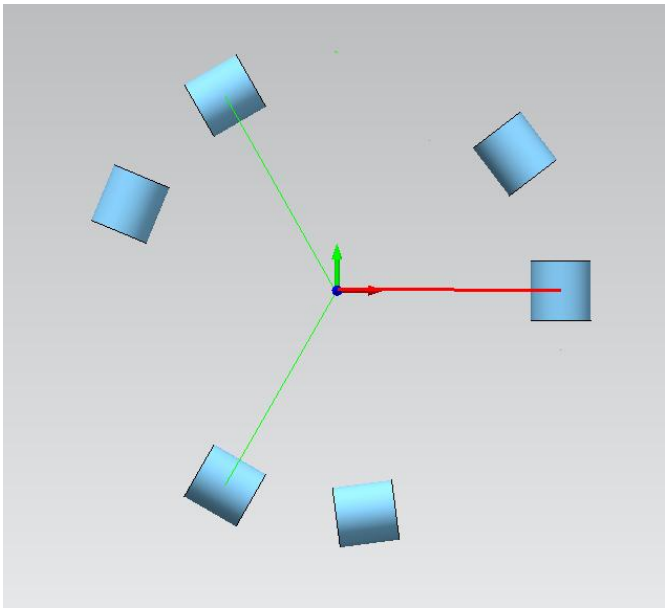

Figure 18 : Simulation of the NES using Simcenter Magnet.

In conclusion, the three magnets will add up to a ~0.3 Nm restoring torque around the center of the axis when they are closest to one of the static magnets.

Using MATLAB's curve fitter, *Eq. 22* becomes:

$$T(\theta) = 1.2701\theta^3 + 0.001\theta \qquad (24)$$

With an R-Squared of 0.978.

4. Experimental Validation

4.1 3D Printing the NES's components

In order to manufacture the body and the arms of the NES, we needed to create two CAD models (*Appendix B)* using NX Siemen's software, one for the rotary system and one for the static system. These CAD models can be seen in *Figure 19*. The center of the magnets is 30mm from the point of symmetry of the solid. Additionally, the static system has an extruded parallelogram over the magnet holder to stop the rotating magnet from getting closer than 4mm to the static magnet.

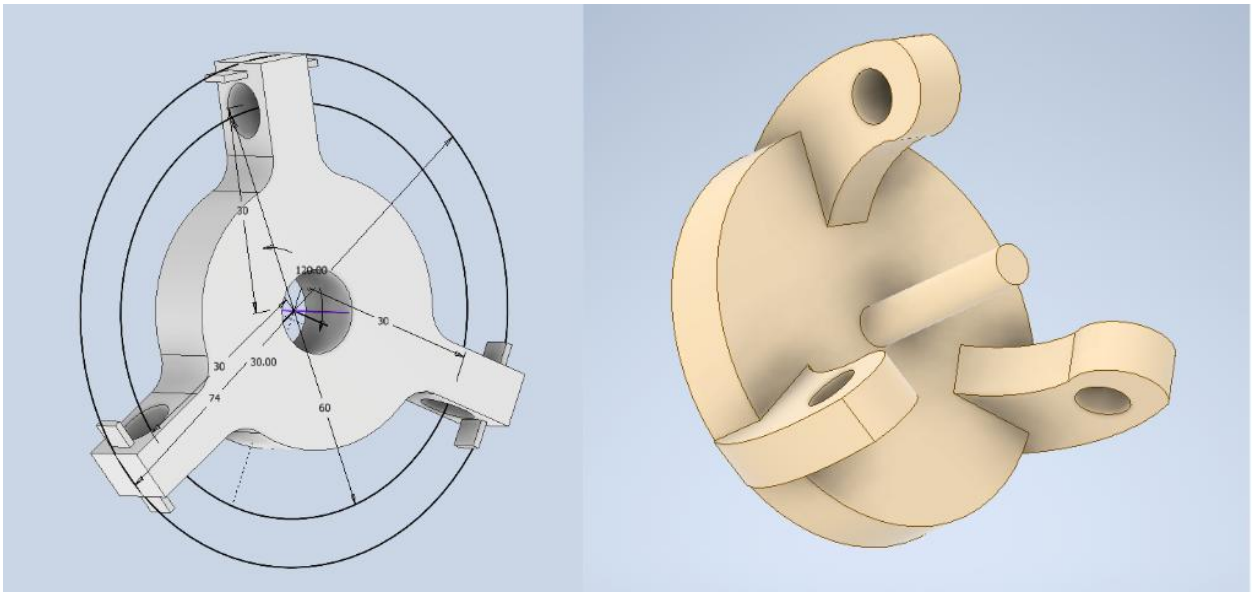

Figure 19 : CAD of the NES's components. LEFT: Stator. Right : Rotor.

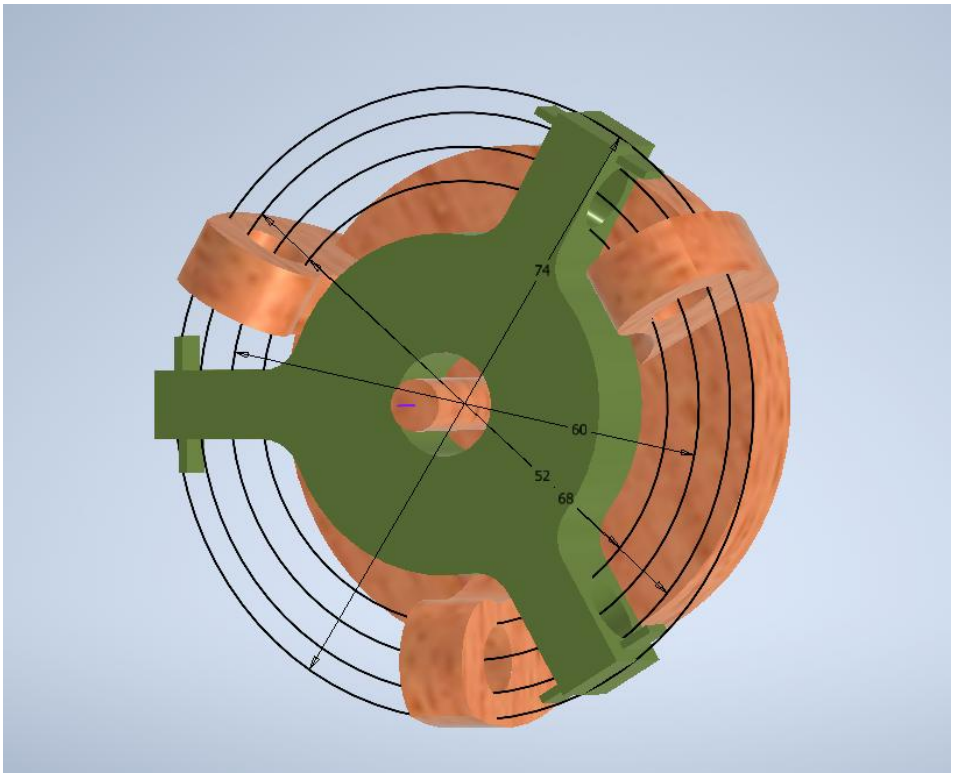

Figure 20 : The assembly of the NES in NX Siemens.

It should be noted that the printing of these parts took about 2 hours to complete. The only problem was that PrusaSlicer had to create a small bridge to the upper part of the holes , where the magnets would be placed in, because it couldn't print the holes otherwise. Also, a surrounding brim was autogenerated by the software in order to make sure that the components don't disconnect from the printer's bed.

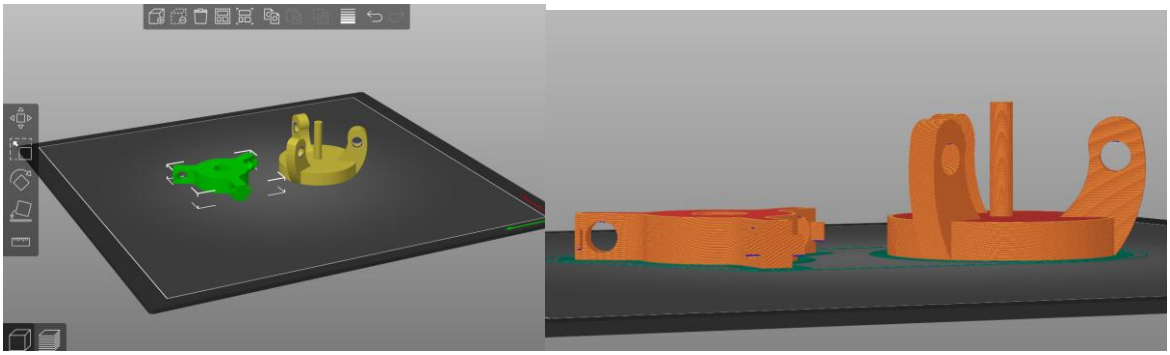

Figure 6 : The components on PrusaSlicer's 3D printing Bed.

Figure 22 : The Raise3D Pro2 Plus 3D printer that was used to print the parts.

The assembly of the NES can be seen in *Figure 23*. The only problem was that because of the imperfections that the printer applied to the holes, a small rasp file was used to clear them out. Also, in order to allign the stator with the rotor we had to apply 3 washers and add a stopper so that the forces don't throw the stator out of the assembly. The stopper and the washers have barely any friction that could diminish the accuracy of the experiments.

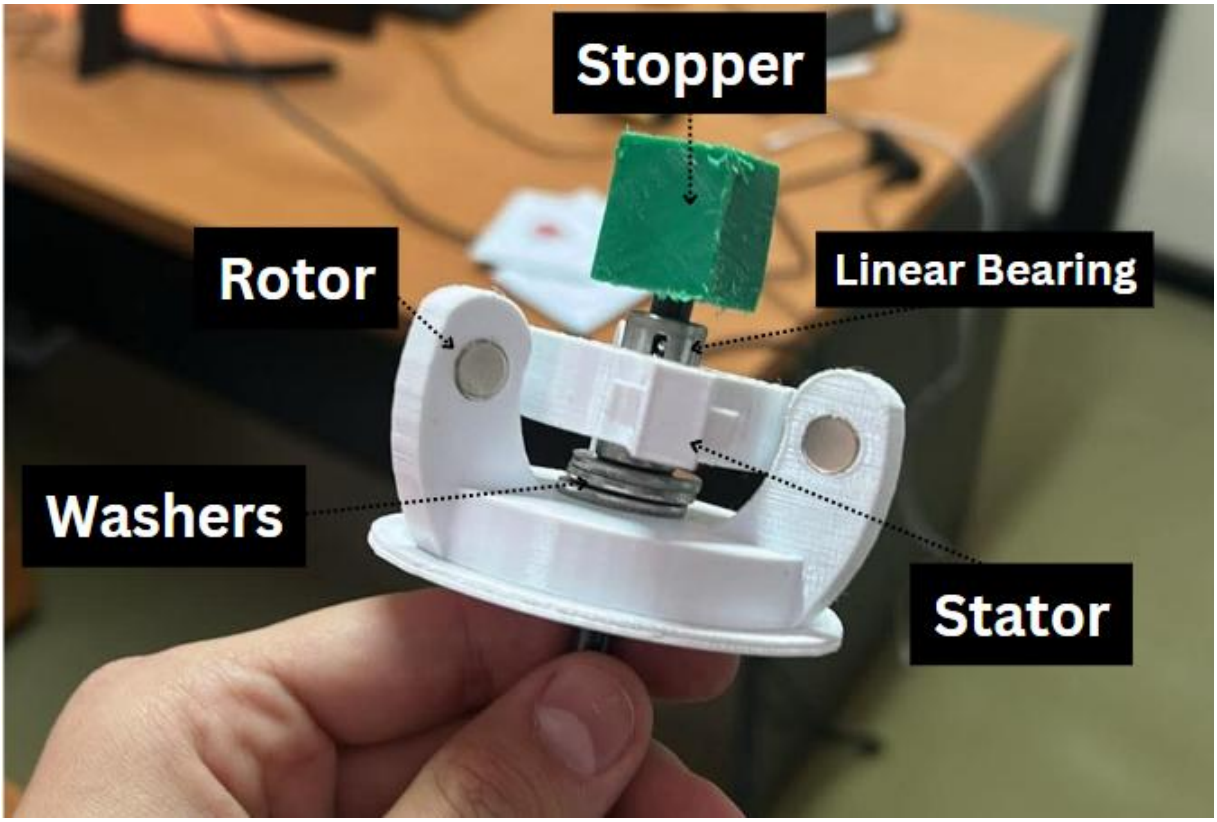

Figure 23 : The NES after assembly.

The properties of the components without the magnets attached to them can be seen in the following table.

Property\Components	Stator	Rotor
Mass (Kg)	0.019	0.042
Principal Moment (x) (Kg*mm^2)	6.853	14.294
Principal Moment (y) (Kg*mm^2)	3.669	14.294
Principal Moment (z) (Kg*mm^2)	3.669	22.737

Table 4 : Properties of the components of the NES.

The moment of inertia (MoI), also known as the mass moment of inertia or angular/rotational mass, of a rigid body is defined relatively to a rotational axis. In our case, it is defined relative to the symmetrical points of each component. MoI defines the ratio between

the torque applied and the resulting angular acceleration about that axis. It plays the same role in rotational motion as mass does in linear motion. A body's MoI about a particular axis depends both on the mass and its distribution relative to the axis [46].

Taking into consideration that the components are not entirely solid and do have some gaps inside them due to the infilling parameter of the printer, their masses and the moments of inertial should change. After calculating the NX Siemen's simulated mass and inertias, then calculating the printed versions of that components and scaling them, we realized that the printed versions weight 46.2% of the simulated mass. If we consider that the density of remains the same on the whole components, then the MoIs should also be 46.2% of their initial values.

In chapter 4.2, the roles of the rotor and the stator will be exchanged. This means that we care mostly about the stator's MoI. So, since we concluded that the final values of the masses are 46.2% of their initial values due to the infill of the 3D printer, we can also calculate the MoI of the moving magnets and add it to the total MoI of the moving component.

$$I_{tot} = I_{stator} + I_{magnets} \; and \; mass_{tot} = mass_{stator} + mass_{magnets} \quad (25)$$

$$I_{tot} = 46.2\% * \begin{bmatrix} 6.853 \\ 3.669 \\ 3.669 \end{bmatrix} + \begin{bmatrix} 8.028 \\ 4.050 \\ 4.050 \end{bmatrix} \text{ and } mass_{tot} = 46.2\% \, mass_{rotor} + mass_{magnets}$$

So the final results for the MoI can be seen in *table 5.*

Property	***Assembly's Value***
Mass (Kg)	***0.019***
Principal Moment (x) (Kg*mm^2)	***11.199***
Principal Moment (y) (Kg*mm^2)	***5.9322***
Principal Moment (z) (Kg*mm^2)	***5.9322***

Table 5 : The Moments of Inertia for the assembly of the rotor and the magnets.

Since the NES will be rotating around the x axis, we only care about the MoI_x = 11.199 kg*mm^2 = 11.199*10^{-6}kg*m^2.

4.2 Experimental Procedure

4.2.1 Dynamic measurements

After printing the components, the performance of the NES needed to be tested. First of all, it was easier to make sure that the stator moves and the rotor stays in place with some M4 bolds and washers. So, the two components exchanged functionalities. The following step was to perform a free vibration test. The stator's magnets were brought as close as possible, not passing the 4mm threshold that was discussed previously, to the magnets of the rotor and let it go, counting the time and keeping track of the angle of the moving magnet. It should be noted that the video was taken at a framerate of 240 frames per second (FPS) so we could basically track 240 angle positions per second. The measurements were made using an Open-Source software called Tracker and the interface of the software can be seen in *Figure 24*. For the tracking, we used the auto-tracking tool by selecting a specific surface that would be easy for the software to keep track of. In order to achieve that, we added a small piece of an orange paper that would break the contrast between the white color of the moving stator and the background.

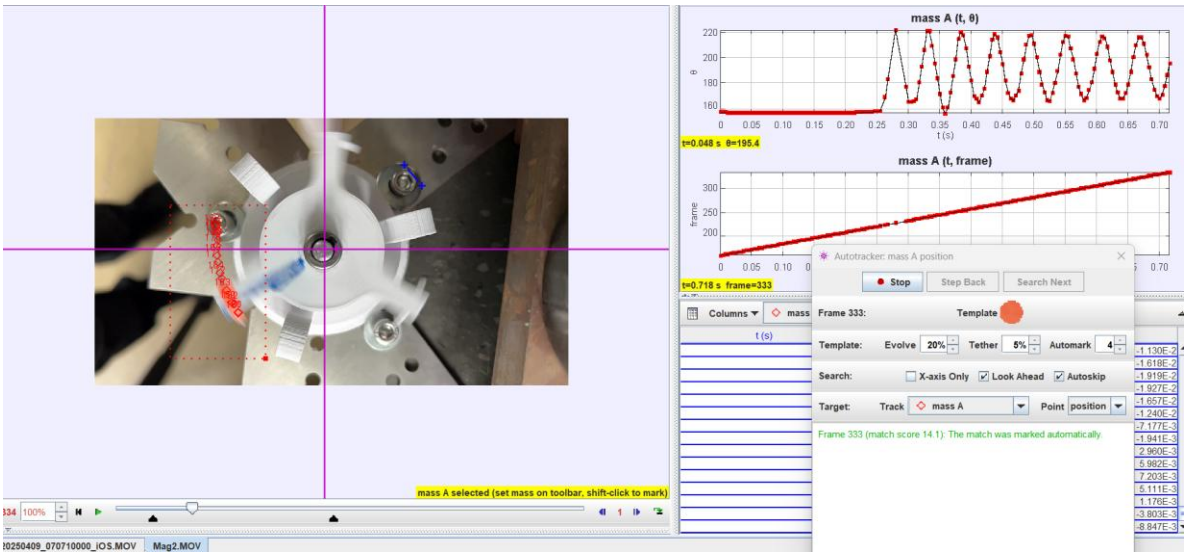

Figure 24 : The interface of the software "Tracker".

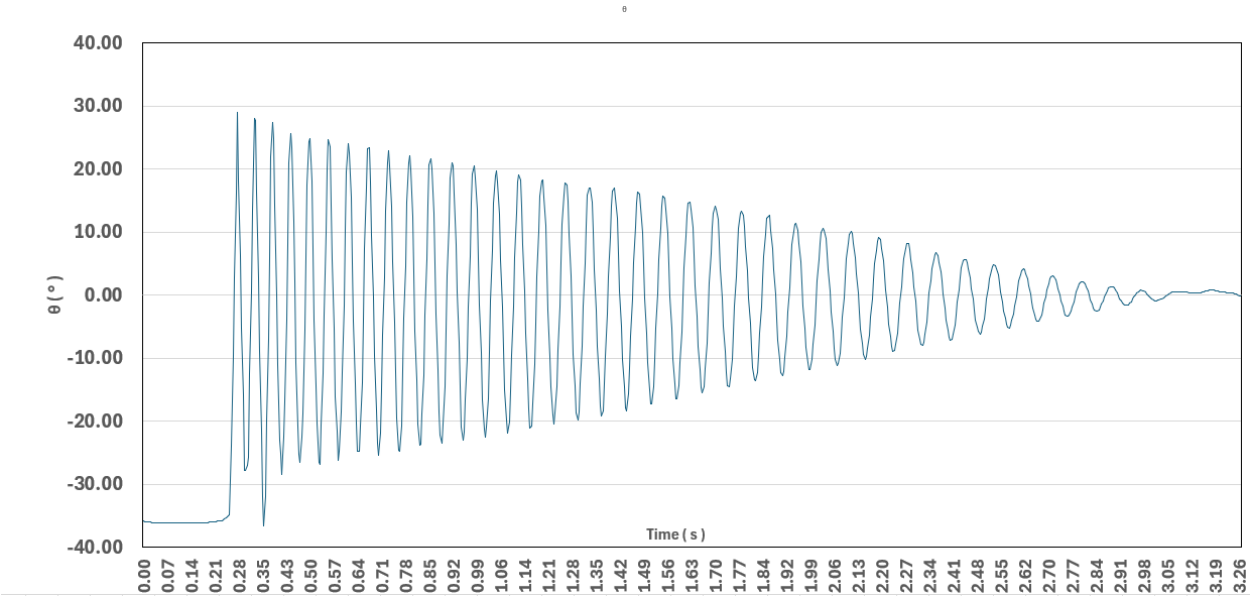

Figure 25 : Measurements of θ (in degrees) from Tracker.

The first few cycles were influenced by small impacts due to the intensity of the magnetic forces and the tolerances of the bearing.. So, all the calculations will take place from t_o = 0.35 seconds to t_f = 2.8 seconds.

Eq. 29, depicts the exponential decay. Through it we are trying to find a damping coefficient C (Ns/m) that would pass through all the local maximums from Figure 25 for the time spam between t_o and t_f .

$$K(t) = \theta(t = t_o) * \exp\left(-c * \frac{t - t_o}{2 * I_{xx}}\right) \qquad t \in [t_o, t_f] \quad (29)$$

The *Eq. 29*'s exponent comes from the damping ratio $\zeta = c/2I_{xx}$. This equation gives us the logarithmic decrement of the measured θ from Tracker.

We concluded that $c = 1 * 10^{-5} \frac{Ns}{m}$ is the best value that fits our experiment. This value is acceptable since this would mean that $\zeta = 0.4504$, that is an acceptable value since it's between 0 and 1 and it is categorized as underdamped. If it was over 1, it would be categorized as overdamped and would not oscillate at all.

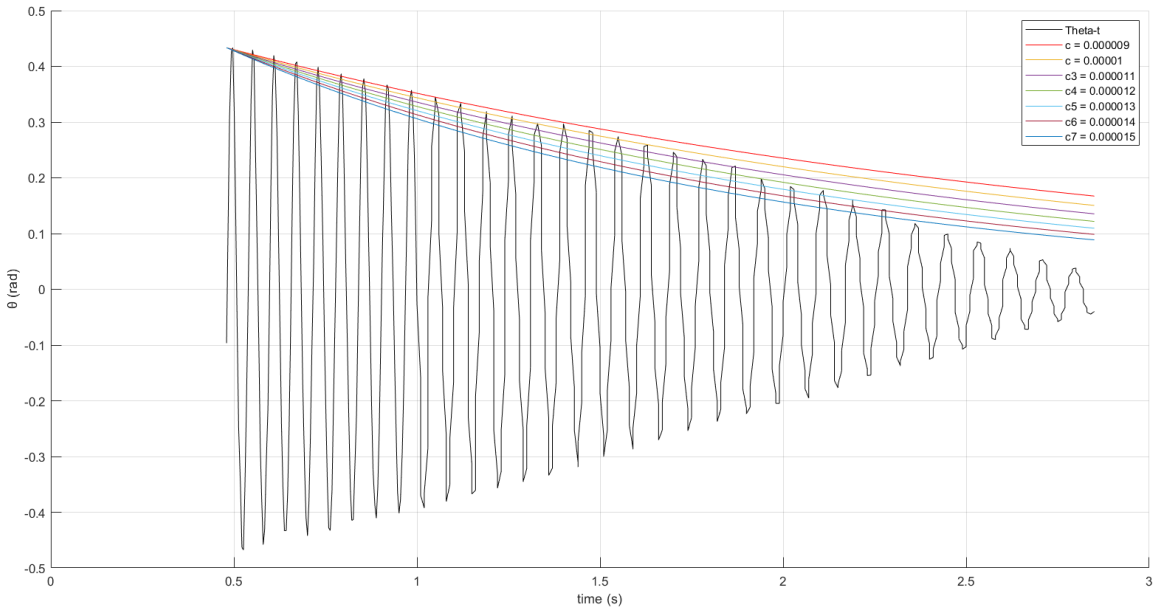

Figure 26 : MATLAB plot of the Tracker's measurements and the $\theta(t = to) * exp(-c(t - to)/2Ixx)$ for different values for c.

From *Figure 26* we conclude that after 1.75 seconds, recorded data departs from the exponential decay which is characteristic of viscous damping. This means that the next simulation of models should take into account dry friction.

4.2.2 Static Measurements

Measuring the restoring torque for the NES was done using a vise to hold the NES's rotor (which turned into the stator) and a hanging platform which was used to add different masses. Figure 27 shows the assembly. After making sure that the arm of the NES is as parallel as possible to the ground, we connected the hanging platform to it, at a distance of 0.035 m from the center of the stator. From the mass that was hanging we measured the restoring force using *Eq. 30.* The results can be seen in *Figure 28 and table 6.* Then, we extrapolated to negative angles by mirroring the restoring torque, thus making it symmetric (*Appendix C.b*) , in order to get a polynomial fitting (PF) in the form of *Eq. 22,* as seen in *Figure 29 and Figure 30*.

$$T(\theta) = m * g * \cos(\theta) * 0.035\ (Nm) \quad (30)$$

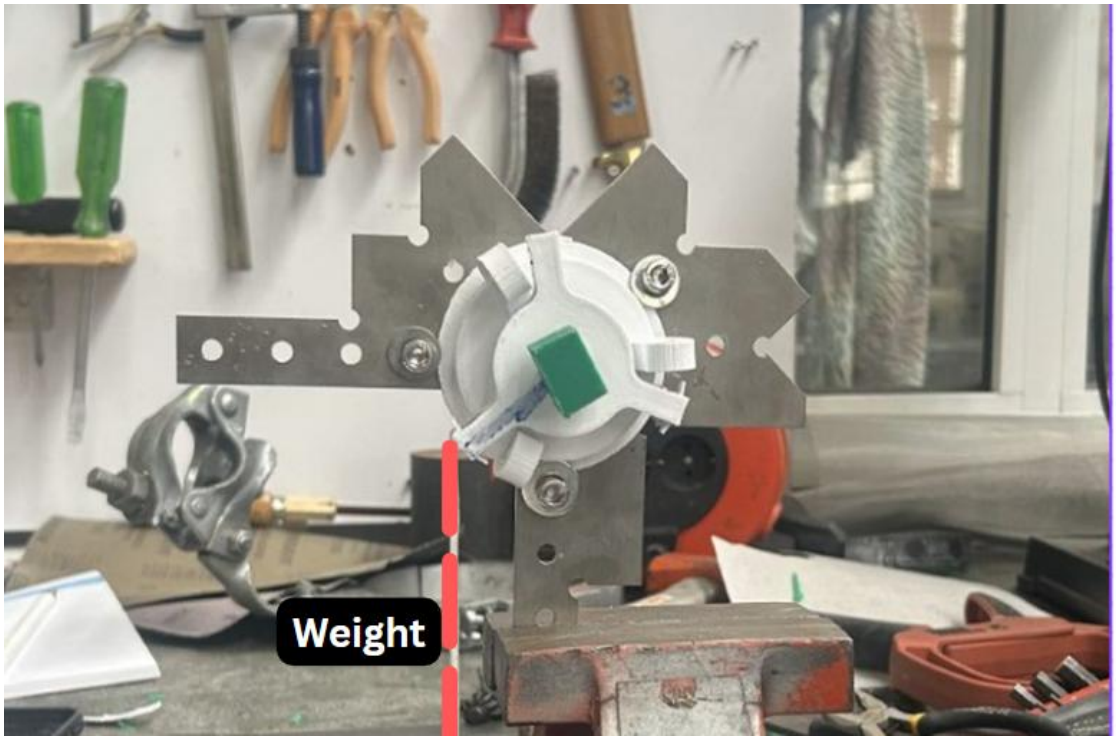

Figure 27 : Measuring the NES's restoring torque using hanging weights.

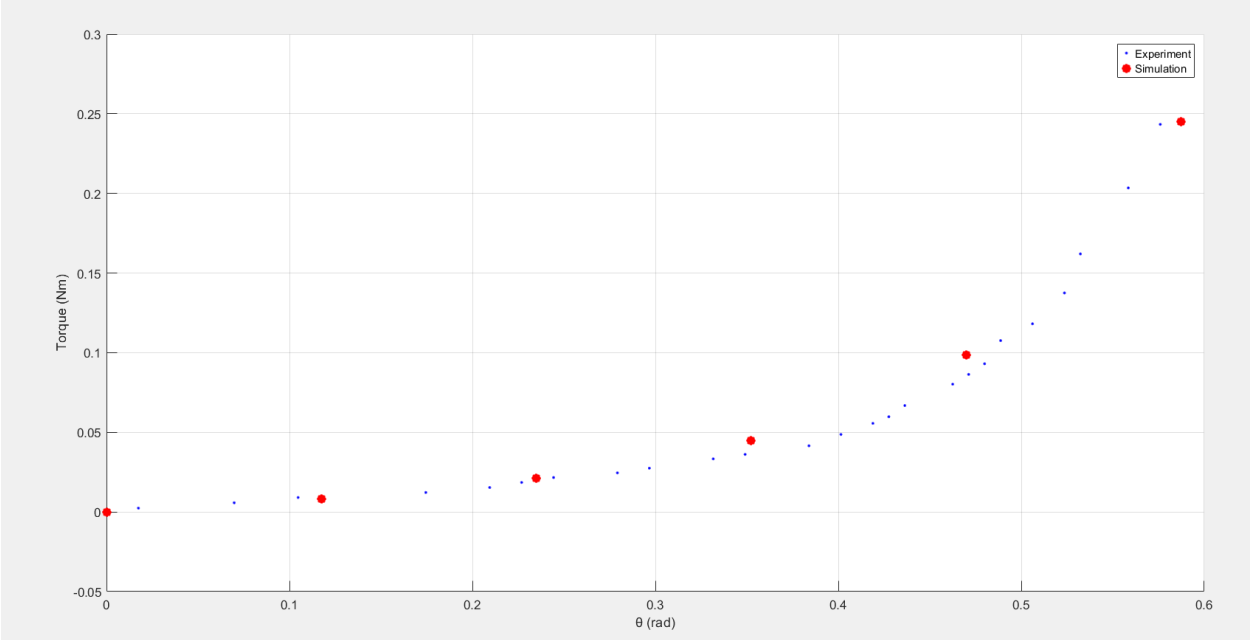

Figure 28 : Restoring Torque(θ) from the experiment and the simulation.

Θ (deg)	Torque (Nm)	Θ (deg)	Torque (Nm)	Θ (deg)	Torque (Nm)
0	0	16	0.024513	26.5	0.080213
1	0.002386	17	0.027497	27	0.086387
4	0.005748	19	0.033296	27.5	0.093052
6	0.009068	20	0.036106	28	0.107598
10	0.012212	22	0.041533	29	0.118127
12	0.015348	23	0.048649	30	0.137499
13	0.018505	24	0.055604	30.5	0.162014
14	0.021617	24.5	0.05976	32	0.203464

Table 6 : Data calculated from the experiment.

From *Figure 28* we can conclude that the experimental restoring torque is very close to the simulated one. This means that the experimental procedure is valid and it can be used in the following experiments.

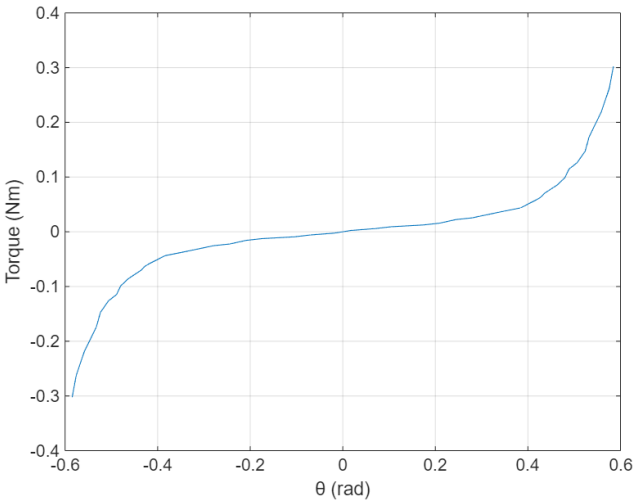

Figure 29: Symmetric Torque around θ = 0 rad.

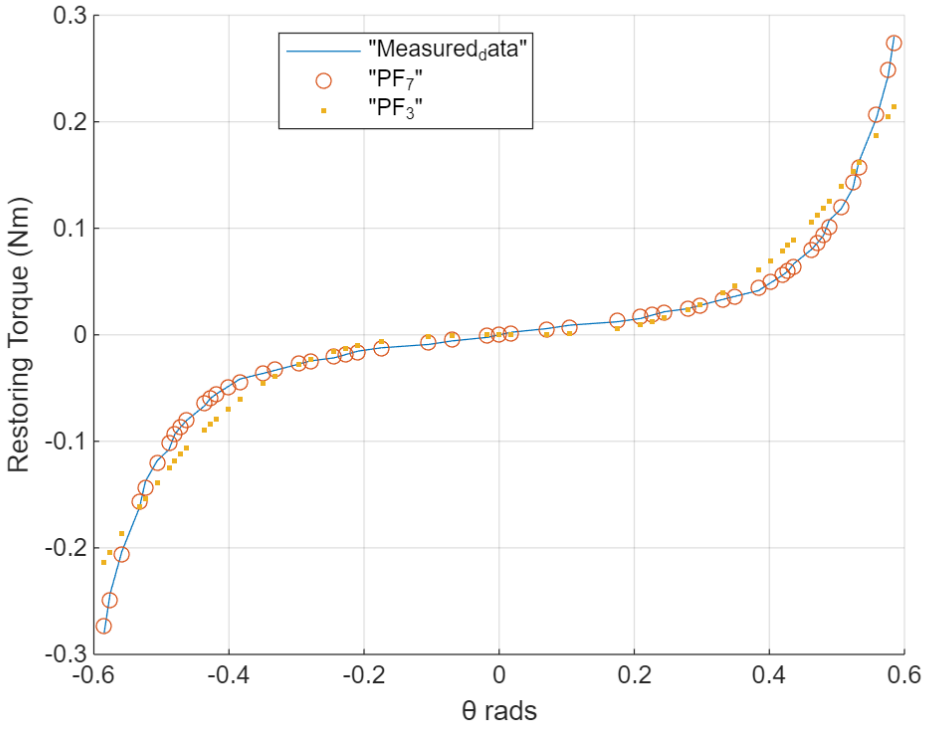

Figure 30 : Fitted restoring Torque from the experiment vs the raw restoring Torque from the experiment. Yellow dots represent the 3rd degree polynomial fitting, and the orange circles represent the 7th degree polynomial fitting.

$$T(\theta) = 1.0682\theta^3 + 0.001\theta \quad (31.a)$$

$$T(\theta) = 14.904\theta^7 - 3.0257\theta^5 + 0.4762\theta^3 + 0.0633\theta \quad (31.b)$$

4.2.3 *Simulating the dynamic system with the restoring torque from the static experiment*

Eq. 31.a gives us a 3rd degree polynomial fitting that is very close to the simulated data and has an R squared of 0.9563. *Eq 31.b* gives us a 7th degree polynomial fitting that even if it's not in the same order as the simulated fitting, it has greater accuracy in representing the restoring torque of the static test with an R squared of 0.998. We will compare the two restoring torques in chapter 4.3.

It should be noted that the experiment does not include the full potential of the NES since it did not reach amplitudes larger than ~30 degrees. After fitting the torque, we used MATLAB (*Appendix C.a*) to simulate a free vibration system comparing it with the 3rd degree

PF's stiffness vs the theoretical (Simcenter Magnet's) stiffness and the experimental data using the *Eq. 32*.

$$Ixx * \ddot{\theta} + c * \dot{\theta} + T(\theta) = 0 \quad (32)$$

Where I_{xx} is the Moment of Inertia that was calculated previously, c = $1*10^{-5}$ Ns/m and $T(\theta)$ are SimCenter Magnet's restoring torque and the experiment's fitted torque.

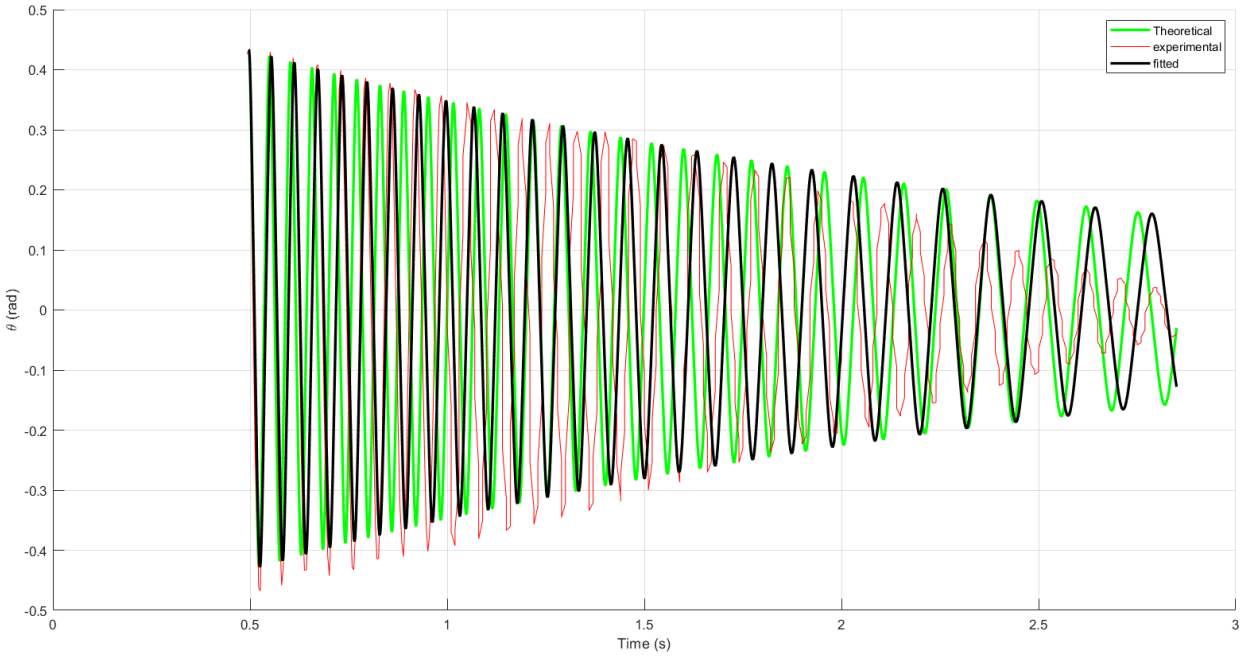

Figure 31 : Theoretical vs Experimental vs Fitted θ.

Figure 31 represents the θ - t plot of the Simulated stiffness of the restoring torque (labeled as "Theoretical"), the *Eq. 31.a* (labeled as "fitted") and the measured θ from Tracker. We concluded that the static restoring torque is valid even for the dynamic system. However, for low amplitudes, it can be observed that the friction between the rotor and the stator is not negligible, so it needs to be taken into consideration. The Translational Friction block represents friction in contact between moving bodies. The friction force is simulated as a function of relative velocity and is assumed to be the sum of Stribeck, Coulomb, and viscous components. The exponential function used in the Stribeck portion of the force equation is continuous and decays at velocity magnitudes greater than the breakaway friction velocity. By taking into consideration the dry friction by using MATLAB's Translation Friction equations (https://www.mathworks.com/help/simscape/ref/translationalfriction.html), implementing it into the equations of the system as seen in *Appendix C.d,* we can see the results in *Figure 32.* We

use rad/s as the Y-axis instead of θ (rads) since the translational friction is relative to velocity and not θ, as seen in *Eq. 33*.

$$\mathrm{F} = \sqrt{2e}\,(F_{brk} - F_c)e^{-\left(\frac{v}{v_{st}}\right)^2}\frac{v}{v_{st}} + F_c \tanh\left(\frac{v}{v_{Coul}}\right) + f_v \qquad (33)$$

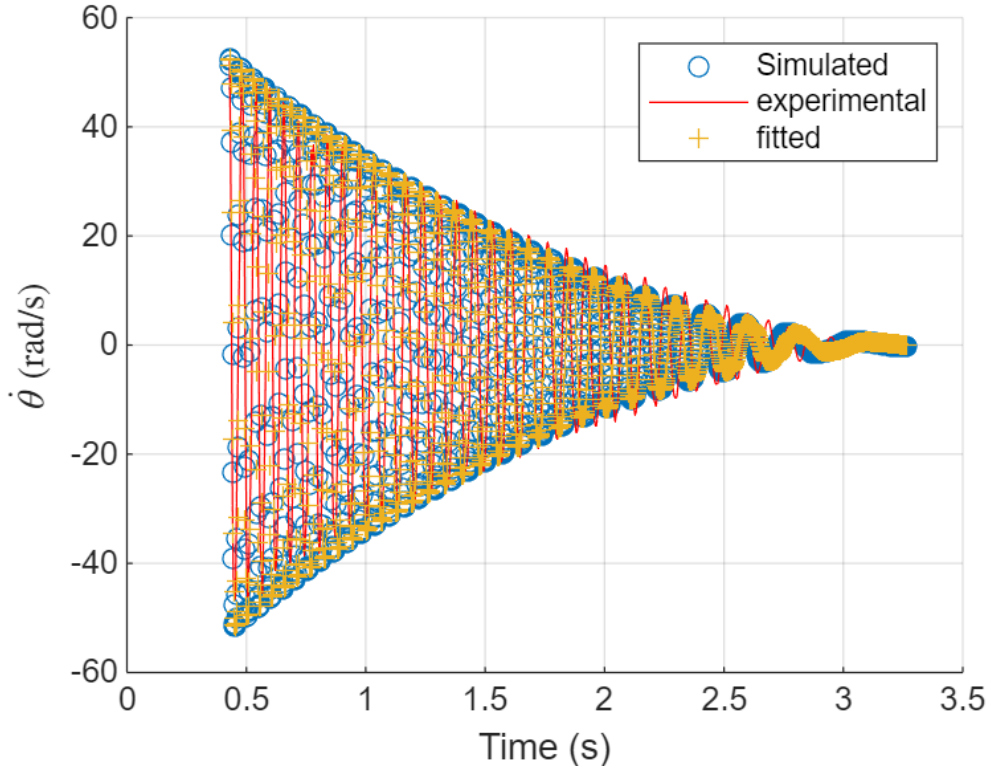

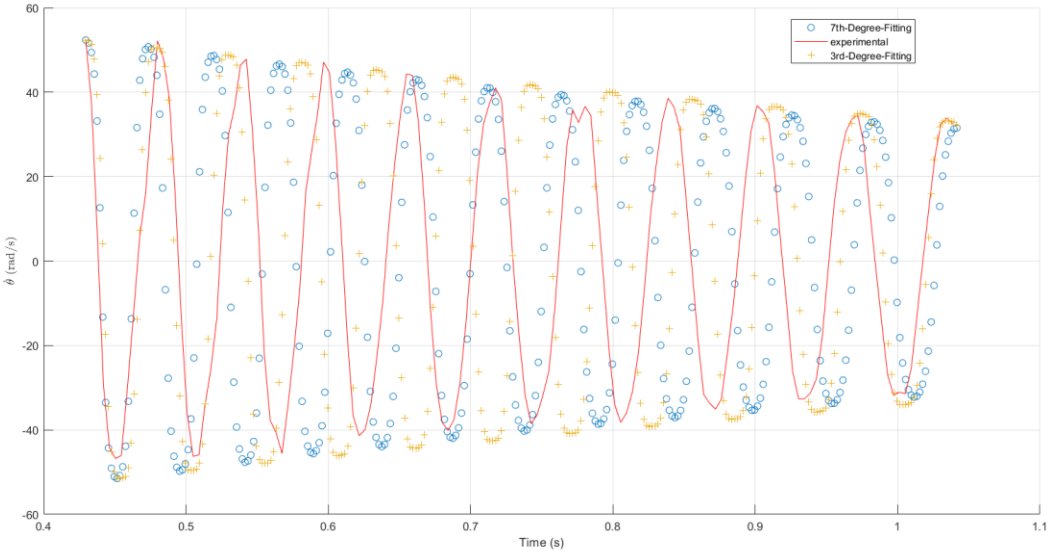

Figure 32 : A plot of the free vibration system vs the 3rd degree fitting from the static experiment and the theoretical fitting from the Simcenter Magnet's simulation of the restoring torque.

Taking into consideration the dry friction of the NES, we conclude that the free vibrating system's (FVS) plot is much more reliable than the one from *Figure 31*. For MATLAB's translation friction equations, we used the values from table 7. As a conclusion, the 3rd degree restoring torque's values from the static experiment are valid and should be taken into consideration.

Variable	Value
Coulomb Friction (F_c)	9N
Breakaway Friction (F_{brk})	14N
Breakaway Velocity threshold (v_{brk})	15 rad/s
Coulomb Velocity threshold (v_c)	v_{brk} / 10
Stribeck Velocity threshold (v_{st})	$1.414v_{brk}$

Table 7 : Variables for MATLAB's Translation Friction equations.

4.3 Comparing the 3rd degree polynomial fitting with the 7th degree polynomial fitting.

Since the 7th degree fitting for the restoring torque, that was measured in the static experiment, seems to fit the restoring torque more accurately than the 3rd degree PF does, we wanted to compare the FVS from *Eq. 32,* that has *Eq. 31.b and Eq. 31.a* as the restoring torques.

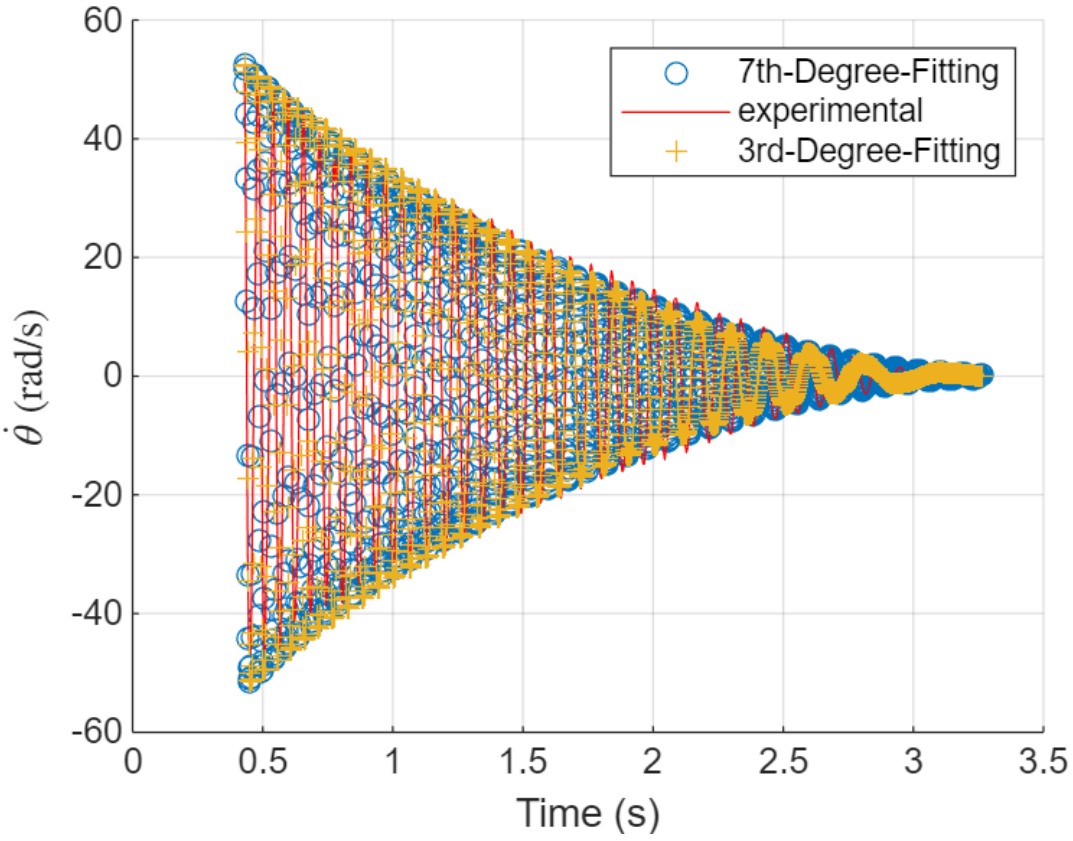

Figure 33 : Plot of the experiment's $\dot{\theta}$– t and the two fitted restoring torques.

From *Figure 33* we conclude that the 3rd degree fitting of the restoring torque can be trusted for torsional vibrations with amplitude of the angular velocity of at least 18 rads/sec.

5. Conclusion

The conclusion of this thesis is that the Nonlinear Energy Sink that was developed, is a powerful tool to absorb unwanted energy from a vibrating system and came really close to the simulated NES. First of all, chapter 3.1 showed that the effects that two magnets have when they are opposing each other and are really close needs extremely precise measuring tools in order to measure the interacting force between them. Thus, for measurements of less than 4 mm, we could not measure the exact interaction between the two magnets. Through the simulations that were done in chapter 3.2, we came to the conclusion that for R=30mm, θ = 120 degrees, we have the least linear and highest nonlinear component of the restoring torque as well as the most reliable fitting from MATLAB's curve fitter.

Chapter 4.1 showed us that the manufactured NES's characteristics, like the moment of inertia or the linear and nonlinear component of the restoring torque differ from the simulated

version of them, perhaps because of unknown variables that were not taken into consideration when the simulations were made. Even though the FVS from *Eq. 32*, with a restoring torque that's fitted with a 3rd degree order, could not be trusted for vibrations with an amplitude of angular velocity less than 18 rad/sec, the 7th degree fitting could be trusted. Also, we came to the realization that dry friction is extremely important for angular velocities that are less than 20 rad/s since the friction that is applied to the NES cannot be ignored. But after taking that friction into account, the simulations came really close to the measured values for θ and $\dot{\theta}$. The thesis was a success since the 3D printed NES's dynamic properties validate the theoretical predictions. The restoring torque for each fitting as well as the simulated one, can be seen bellow.

$$T(\theta) = 1.0682\theta^3 + 0.001\theta \, , 3rd\ degree\ fitting$$

$$T(\theta) = 14.904\theta^7 - 3.0257\theta^5 + 0.4762\theta^3 + 0.0633\theta \, , 7th\ degree\ fitting$$

$$T(\theta) = \ 1.2701\theta^3 + 0.001\theta \, , Simulated\ Restoring\ torque$$

6. Future Work

A good idea for future work is to simulate the interaction between the stator and the rotor by taking into account as many variables as possible. For example, by adding to the simulation the linear bearing that was used to allow the rotor to rotate along the stator, or the friction that there was between the bearing and the components of the NES, the simulations could be more accurate and represent better the real-life scenario. Also, future research should try to use the full potential of the NES by bringing the stator's and rotor's magnets as close as possible to each other for the dynamic experiment, taking advantage of the whole restoring torque pf the NES. Another good idea would be to use high speed cameras that automatically track the angle and the angular speed at which the rotor of the NES rotates and export this data automatically to an Excel sheet. Also, more tests can be done with the developed NES in a more realistic scenario to evaluate the attenuation performance of the contactless NES.

References

[1] Classens, K., Schoukens, M., Oomen, T., & Noël, J.-P. (2025). Locating nonlinearities in mechanical systems: A frequency-domain dynamic network perspective. *Mechanical Systems and Signal Processing*, *224*, 112124. https://doi.org/10.1016/j.ymssp.2024.112124

[2] Chu, T., Nguyen, T., Yoo, H., & Wang, J. (2024). A review of vibration analysis and its applications. *Heliyon*, *10*(5), e26282. https://doi.org/10.1016/j.heliyon.2024.e26282

[3] Ding, H., & Chen, L.-Q. (2020). Designs, analysis, and applications of nonlinear energy sinks. *Nonlinear Dynamics*, *100*(4), 3061–3107. https://doi.org/10.1007/s11071-020-05724-1

[4] Hrovat, D., Barak, P., & Rabins, M. (1983). Semi-Active versus Passive or Active Tuned Mass Dampers for Structural Control. *Journal of Engineering Mechanics*, *109*(3), 691–705. https://doi.org/10.1061/(ASCE)0733-9399(1983)109:3(691)

[5] Koutsoloukas, L., Nikitas, N., & Aristidou, P. (2022). Passive, semi-active, active and hybrid mass dampers: A literature review with associated applications on building-like structures. *Developments in the Built Environment*, *12*, 100094. https://doi.org/10.1016/j.dibe.2022.100094

[6] Lee, I.-W., Kim, D.-O., & Jung, G.-H. (1999). NATURAL FREQUENCY AND MODE SHAPE SENSITIVITIES OF DAMPED SYSTEMS: PART I, DISTINCT NATURAL FREQUENCIES. *Journal of Sound and Vibration*, *223*(3), 399–412. https://doi.org/10.1006/jsvi.1998.2129

[7] Shahzad, U. (2015). *Global Warming: Causes, Effects and Solutions*.

[8] Gatasheh, M. K., Abbas, T., shaffique, S., Kang, S.-M., Lee, I.-J., & shah, A. A. (2025). Comparative analysis of biodiversity, physiology, and anatomical adaptations in riparian flora exposed to industrial pollution stress. *Scientific Reports*, *15*(1), 3006. https://doi.org/10.1038/s41598-025-87396-8

[9] Szabó, J. Z., & Dömötör, F. (2023). *Comparative Testing of Vibrations in Vehicles Driven by Electric Motor and Internal Combustion Engine (ICE)* (pp. 871–879). https://doi.org/10.1007/978-3-031-15211-5_72

[10] Saha, N., Panda, A. K., & Panda, S. (2018). Speed control with torque ripple reduction of switched reluctance motor by many optimizing liaison technique. *Journal of Electrical Systems and Information Technology*, *5*(3), 829–842. https://doi.org/10.1016/j.jesit.2016.12.013

[11] Gulez, K., Adam, A. A., & Pastaci, H. (2008). Torque Ripple and EMI Noise Minimization in PMSM Using Active Filter Topology and Field-Oriented Control. *IEEE Transactions on Industrial Electronics*, *55*(1), 251–257. https://doi.org/10.1109/TIE.2007.896295

[12] Tiemessen, I. J. H., Hulshof, C. T. J., & Frings-Dresen, M. H. W. (2008). Low back pain in drivers exposed to whole body vibration: analysis of a dose–response pattern. *Occupational and Environmental Medicine*, *65*(10), 667–675. https://doi.org/10.1136/oem.2007.035147

[13] Kadmiri, Y., Rigaud, E., Perret-Liaudet, J., & Vary, L. (2012). Experimental and numerical analysis of automotive gearbox rattle noise. *Journal of Sound and Vibration*, *331*(13), 3144–3157. https://doi.org/10.1016/j.jsv.2012.02.009

[14] Masri, J., Amer, M., Salman, S., Ismail, M., & Elsisi, M. (2024). A survey of modern vehicle noise, vibration, and harshness: A state-of-the-art. *Ain Shams Engineering Journal*, *15*(10), 102957. https://doi.org/10.1016/j.asej.2024.102957

[15] Yüksel, C. (2017). The Use of Neodymium Magnets in Healthcare and Their Effects on Health. *Northern Clinics of Istanbul*. https://doi.org/10.14744/nci.2017.00483

[16] Shewane, P. G., Gite, M., & Singh, A. (n.d.). *International Journal on Recent and Innovation Trends in Computing and Communication An Overview of Neodymium Magnets over Normal Magnets for the Generation of Energy*. http://www.ijritcc.org

[17] Diez-Jimenez, E., Perez-Diaz, J. L., Ferdeghini, C., Canepa, F., Bernini, C., Cristache, C., Sanchez-Garcia-Casarrubios, J., Valiente-Blanco, I., Ruiz-Navas, E. M., & Martínez-Rojas, J. A. (2018). Magnetic and morphological characterization of Nd2Fe14B magnets with different quality grades at low temperature 5–300 K. *Journal of Magnetism and Magnetic Materials*, *451*, 549–553. https://doi.org/10.1016/j.jmmm.2017.11.109

[18] A. F. Vakakis, O. V. Gendelman, L. A. Bergman, D. M. McFarland, G. Kerschen, & Y. S. Lee. (2009). *Nonlinear Targeted Energy Transfer in Mechanical and Structural Systems* (Vol. 156). Springer Netherlands. https://doi.org/10.1007/978-1-4020-9130-8

[19] Li, W., Wierschem, N. E., Li, X., & Yang, T. (2018). On the energy transfer mechanism of the single-sided vibro-impact nonlinear energy sink. *Journal of Sound and Vibration*, *437*, 166–179. https://doi.org/10.1016/j.jsv.2018.08.057

[20] Holmes, J. D. (1995). Listing of installations. *Engineering Structures*, *17*(9), 676–678. https://doi.org/10.1016/0141-0296(95)90027-6

[21] Saeed, A. S., Abdul Nasar, R., & AL-Shudeifat, M. A. (2023). A review on nonlinear energy sinks: designs, analysis and applications of impact and rotary types. *Nonlinear Dynamics*, *111*(1), 1–37. https://doi.org/10.1007/s11071-022-08094-y

[22] Gendelman, O. v. (2001). Transition of Energy to a Nonlinear Localized Mode in a Highly Asymmetric System of Two Oscillators. *Nonlinear Dynamics*, *25*(1/3), 237–253. https://doi.org/10.1023/A:1012967003477

[23] Vakakis, A. F., Manevitch, L. I., Gendelman, O., & Bergman, L. (2003). Dynamics of linear discrete systems connected to local, essentially non-linear attachments. *Journal of Sound and Vibration*, *264*(3), 559–577. https://doi.org/10.1016/S0022-460X(02)01207-5

[24] Gourdon, E., Alexander, N. A., Taylor, C. A., Lamarque, C. H., & Pernot, S. (2007). Nonlinear energy pumping under transient forcing with strongly nonlinear coupling: Theoretical and experimental results. *Journal of Sound and Vibration*, *300*(3–5), 522–551. https://doi.org/10.1016/j.jsv.2006.06.074

[25] Jiang, X., McFarland, D. M., Bergman, L. A., & Vakakis, A. F. (2003). Steady State Passive Nonlinear Energy Pumping in Coupled Oscillators: Theoretical and Experimental Results. *Nonlinear Dynamics*, *33*(1), 87–102. https://doi.org/10.1023/A:1025599211712

[26] Jin, Y., Liu, K., Xiong, L., & Tang, L. (2022). A non-traditional variant nonlinear energy sink for vibration suppression and energy harvesting. *Mechanical Systems and Signal Processing*, *181*, 109479. https://doi.org/10.1016/j.ymssp.2022.109479

[27] Lee, Y. S., Kerschen, G., Vakakis, A. F., Panagopoulos, P., Bergman, L., & McFarland, D. M. (2005). Complicated dynamics of a linear oscillator with a light, essentially nonlinear attachment. *Physica D: Nonlinear Phenomena*, *204*(1–2), 41–69. https://doi.org/10.1016/j.physd.2005.03.014

[28] Yang, H., Yang, B., Wang, H., Zhang, M., & Ni, S. (2022). Research on Dynamic Characteristics of Joint of RC Frame Structure with NES. *Sustainability*, *14*(18), 11229. https://doi.org/10.3390/su141811229

[29] Jamali, M., Mehta, K. S., Holweger, H., Amrei, M. M., & Tafreshi, H. v. (2021). Controlling detachment residue via magnetic repulsion force. *Applied Physics Letters*, *118*(19). https://doi.org/10.1063/5.0052141

[30] Grebenikov, V. v., Gamaliia, R. v., Chumak, V. v., Sotnyk, M. I., & Popkov, V. S. (2024). Analysis of Permanent Magnet Motor Magnetic System Configurations for a Borehole Pump. *2024 IEEE 7th International Conference on Smart Technologies in Power Engineering and Electronics (STEE)*, TT1.03.1-TT1.03.6. https://doi.org/10.1109/STEE63556.2024.10748023

[31] Cooper, R., Neil, V., & Woodruff, W. (1973). Optimum permanent-magnet dimensions for repulsion applications. *IEEE Transactions on Magnetics*, *9*(2), 125–127. https://doi.org/10.1109/TMAG.1973.1067575

[32] Hernandez, W. (2006). Improving the Response of a Load Cell by Using Optimal Filtering. *Sensors*, *6*(7), 697–711. https://doi.org/10.3390/s6070697

[33] Badamasi, Y. A. (2014). The working principle of an Arduino. *2014 11th International Conference on Electronics, Computer and Computation (ICECCO)*, 1–4. https://doi.org/10.1109/ICECCO.2014.6997578

[34] Shahrubudin, N., Lee, T. C., & Ramlan, R. (2019). An Overview on 3D Printing Technology: Technological, Materials, and Applications. *Procedia Manufacturing*, *35*, 1286–1296. https://doi.org/10.1016/j.promfg.2019.06.089

[35] Madhavan Nampoothiri, K., Nair, N. R., & John, R. P. (2010). An overview of the recent developments in polylactide (PLA) research. *Bioresource Technology*, *101*(22), 8493–8501. https://doi.org/10.1016/j.biortech.2010.05.092

[36] Hao Wen, Jing Ma, Meiju Zhang, & Guimei Ma. (2012). The comparison research of nonlinear curve fitting in Matlab and LabVIEW. *2012 IEEE Symposium on Electrical & Electronics Engineering (EEESYM)*, 74–77. https://doi.org/10.1109/EEESym.2012.6258591

[37] Chicco, D., Warrens, M. J., & Jurman, G. (2021). The coefficient of determination R-squared is more informative than SMAPE, MAE, MAPE, MSE and RMSE in regression analysis evaluation. *PeerJ Computer Science*, *7*, e623. https://doi.org/10.7717/peerj-cs.623

[38] Wang, T., & Ding, Q. (2023). Targeted energy transfer analysis of a nonlinear oscillator coupled with bistable nonlinear energy sink based on nonlinear normal modes. *Journal of Sound and Vibration*, *556*, 117727. https://doi.org/10.1016/j.jsv.2023.117727

[39] Mackay, R. S., Meiss, J. D., & Percival, I. C. (1984). Transport in Hamiltonian systems. *Physica D: Nonlinear Phenomena*, *13*(1–2), 55–81. https://doi.org/10.1016/0167-2789(84)90270-7

[40] Tsakirtzis, S., Panagopoulos, P. N., Kerschen, G., Gendelman, O., Vakakis, A. F., & Bergman, L. A. (2007). Complex dynamics and targeted energy transfer in linear oscillators coupled to multi-degree-of-freedom essentially nonlinear attachments. *Nonlinear Dynamics*, *48*(3), 285–318. https://doi.org/10.1007/s11071-006-9089-x

[41] Lee, Y. S., Kerschen, G., Vakakis, A. F., Panagopoulos, P., Bergman, L., & McFarland, D. M. (2005). Complicated dynamics of a linear oscillator with a light, essentially nonlinear attachment. *Physica D: Nonlinear Phenomena*, *204*(1–2), 41–69. https://doi.org/10.1016/j.physd.2005.03.014

[42] Al-Shudeifat, M. A., & Saeed, A. S. (2022). Periodic Motion and Frequency Energy Plots of Dynamical Systems Coupled With Piecewise Nonlinear Energy Sink. *Journal of Computational and Nonlinear Dynamics*, *17*(4). https://doi.org/10.1115/1.4053509

[43] Haris, A., Alevras, P., Mohammadpour, M., Theodossiades, S., & O' Mahony, M. (2020). Design and validation of a nonlinear vibration absorber to attenuate torsional oscillations of propulsion systems. *Nonlinear Dynamics*, *100*(1), 33–49. https://doi.org/10.1007/s11071-020-05502-z

[44] J. Went, G.W. Rathenau, E.W. Gorter, G.W. van Oosterhout
Physical Review, 86 (1951), p. 424

[45] Adam, A. (2022). Structural and Magnetic Properties of Dy Doped Sr1-Xdyxfe12o19 Ferrites. *SSRN Electronic Journal*. https://doi.org/10.2139/ssrn.4203163

[46] Bächer, M., Whiting, E., Bickel, B., & Sorkine-Hornung, O. (2014). Spin-it. *ACM Transactions on Graphics*, *33*(4), 1–10. https://doi.org/10.1145/2601097.2601157

Appendix A – Arduino Script

1. Arduino's script for measuring the force applied to the lower magnet by the moving magnet in *chapter 3.1.2 .*
2. #include "HX711.h" // *We are using this library in order to set up the Load Cell and function it as a scale.*
3. #define DT_PIN 3 // HX711 data pin
4. #define SCK_PIN 2 // HX711 clock pin // *The Load Cell, apart from the power in and ground pins, it also has two pins to read the data.*
5. HX711 scale; // *We use this to define the Load Cell as a scale.*
6. void setup() {
7. Serial.begin(9600);
8. scale.begin(DT_PIN, SCK_PIN);
9. *// Calibrate the scale with a known weight before using*
10. scale.set_scale(430.f); *// Adjusting this number in order to get accurate readings from the Load Cell.*
11. scale.tare(); // Reset scale to zero
12. }
13. void loop() {
14. float measured_mass_g = scale.get_units(); *// Mass in grams*
15. float measured_mass_kg = measured_mass_g / 1000.0; *// Convert to kg*
16. float force_N = measured_mass_kg * 9.81; *// Convert to Newtons*
17. Serial.println(force_N); *// Displaying the results on the command prompt.*
18. delay(100); // waiting for 0.1 seconds.
19. }

Appendix B – CAD

CAD Drawings of the two components that make up the NES.

Stator

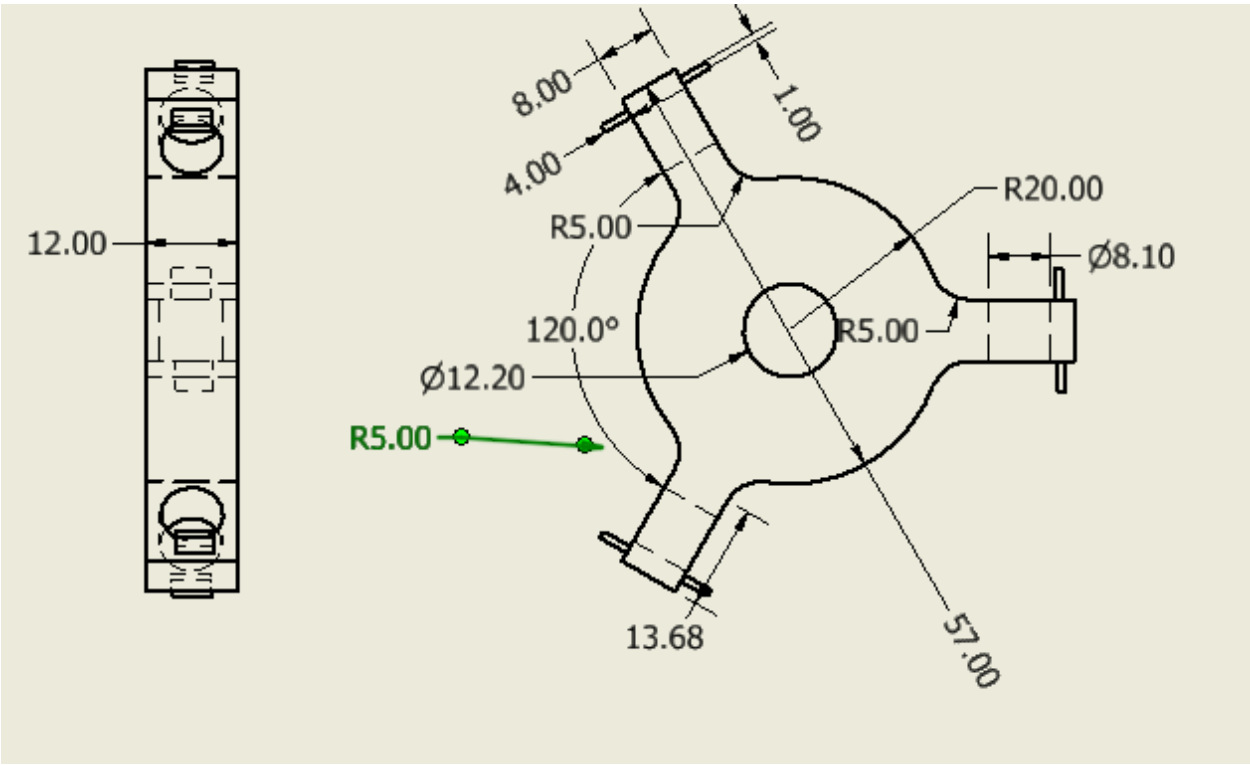

Rotor

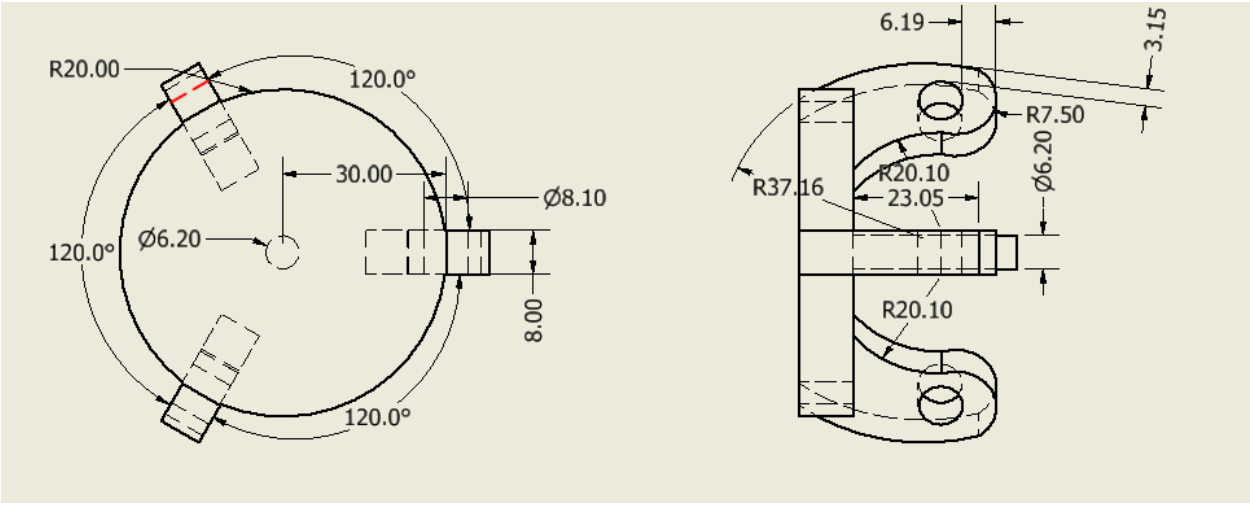

Appendix C – MATLAB

a) Script for comparing the θ-t plots

```
clc
clear %Clearing the environment and all the variables
load("ThetaTime.mat") %Loading Tracker's θ and time.
theta_0 = theta(5); %Starting from the 5th value of Tracker's θ which is the first peak that we care about
time_0 = time(5);
time_f = time(end);
theta_dot_0 = 0;
k_l_exp = 0.001;
k_nl_exp = 1.0682;
k_l_theoretical = 0.001;
k_nl_theoretical = 1.2701;
Ix = 11.599*10^(-6);
c = 0.000015; %Declaring all the essential variables
t_span = [time_0,time_f];
InitialCond = [theta_0,theta_dot_0];
[t_1,theta_1] = ode45(@(t,theta_1) theta_system(t,theta_1,Ix,c,k_l_theoretical,k_nl_theoretical),t_span,InitialCond);
[t_2,theta_2] = ode45(@(t,theta_2) theta_system(t,theta_2,Ix,c,k_l_exp,k_nl_exp),t_span,InitialCond); %Solving the Eq.32
figure; %plotting the results
hold on;
plot(t_1, theta_1(:,1),'green','LineWidth', 2);
plot(time(4:end),theta(4:end),'red')
plot(t_2,theta_2(:,1),'black','LineWidth',2)
xlabel('Time (s)');
ylabel('\theta (rad)');
legend 'Theoretical' 'experimental' 'fitted'
grid on;
hold off
function dthdt = theta_system(t,theta,Ix,c,k_l,k_nl)
Fc=9;
Fbrk=Fc+5;
vbrk=15;
vst=sqrt(2)*vbrk;
vC=vbrk/10;
dthdt = zeros(2,1);
dthdt(1) = theta(2);
%dthdt(2) = -27*tanh(theta(2)/3) -(c/Ix)*theta(2) - (k_l/Ix)*theta(1) - (k_nl/Ix)*theta(1)^5;
```

```
37. dthdt(2) = -sqrt(2*exp(1))*(Fbrk-Fc)*exp(-(theta(2)/(vst))^2)*(theta(2)/vst)-
    Fc*tanh(theta(2)/vC)-(c/Ix)*theta(2) -(k_nl*theta(1)^3 + k_l*theta(1))/Ix;
38. end
```

b) Script for making the data symmetrical and for comparing it with the fitted version of it

```
1. theta = Data.x_Normal';  % Importing the data from Microsoft Excel.
2. Torque = Data.Nm';
3. theta_sym = deg2rad([-fliplr(theta(theta > 0)) theta]);
4. Torque_sym =  [-fliplr(Torque(Torque > 0)) Torque]; %Making the θ and torque
   symmetrical.
5. %Fitting of the sim data.
6. for i = 1:length(theta_sym)
7. torque_fitted(i) = 1.0682*theta_sym(i)^3 + 0.001*theta_sym(i); % making a vector that
   contains the fitted data .
8. end
9. figure; %Plotting the results in order to compare them.
10. hold on
11. title("Torque from experiment vs Torque fitted")
12. plot(theta_sym,Torque_sym)
13. plot(theta_sym,torque_fitted,'o')
14. xlabel("θ (rad)")
15. ylabel("Torque (Nm)")
16. legend 'Torque Experiment' 'Torque Fitted'
17. grid on;
```

c) Script to post process and fit the Simcenter Magnet's data.

```
1. clc
2. clear %Cleaning the environment of MATLAB and the previous variables
3. R_theta_Torque = readtable('R_theta_Torque.xlsx') %Reading data from the excel
4. %Couling the Torque and the theta for each simulation.
5. R30_Theta90 = [R_Theta_Torque.Theta,R_Theta_Torque.Torque_NM_];
6. R30_Theta90 = R30_Theta90(~any(isnan(R30_Theta90), 2), :) %Remove rows with
   NaN
7. R30_Theta120 = [R_Theta_Torque.Theta1,R_Theta_Torque.Torque_NM_1];
8. R30_Theta120 = R30_Theta120(~any(isnan(R30_Theta120), 2), :)
9. R45_Theta90 = [R_Theta_Torque.Theta2,R_Theta_Torque.Torque_NM_2];
10. R45_Theta90 = R45_Theta90(~any(isnan(R45_Theta90), 2), :)
11. R45_Theta120 = [R_Theta_Torque.Theta3,R_Theta_Torque.Torque_NM_3];
12. R45_Theta120 = R45_Theta120(~any(isnan(R45_Theta120), 2), :)
13. R60_Theta90 = [R_Theta_Torque.Theta4,R_Theta_Torque.Torque_NM_4];
14. R60_Theta90 = R60_Theta90(~any(isnan(R60_Theta90), 2), :)
```

```
R60_Theta120 = [R_Theta_Torque.Theta5,R_Theta_Torque.Torque_NM_5];
R60_Theta120 = R60_Theta120(~any(isnan(R60_Theta120), 2), :)
save('R_ThetaVsTorqueRes','-mat') %Saving the data to not lose it.
%Splitting the data into x and y components ( theta and torque ) to be able to use the fitting tool provided by MATLAB and converting degrees to rads.
R30Th90X = deg2rad(R30_Theta90(:,1) - (max(R30_Theta90(:,1)) + min(R30_Theta90(:,1)))/2) ;
R30Th90Y = R30_Theta90(:,2);
R30Th120X = deg2rad(R30_Theta120(:,1) - (max(R30_Theta120(:,1)) + min(R30_Theta120(:,1)))/2);
R30Th120Y = R30_Theta120(:,2) ;
R45Th90X = deg2rad(R45_Theta90(:,1) - (max(R45_Theta90(:,1)) + min(R45_Theta90(:,1)))/2);
R45Th90Y = R45_Theta90(:,2);
R45Th120X = deg2rad(R45_Theta120(:,1) - (max(R45_Theta120(:,1)) + min(R45_Theta120(:,1)))/2);
R45Th120Y = R45_Theta120(:,2);
R60Th90X = deg2rad(R60_Theta90(:,1) - (max(R60_Theta90(:,1)) + min(R60_Theta90(:,1)))/2);
R60Th90Y = R60_Theta90(:,2);
R60Th120X = deg2rad(R60_Theta120(:,1)- (max(R60_Theta120(:,1)) + min(R60_Theta120(:,1)))/2);
R60Th120Y = R60_Theta120(:,2);
%The results of the fitting for T(θ) = Alpha θ^3 + Beta θ
Alpha = [-0.518 , -0.4339 , -0.9954 , -0.2741 , -0.6493 , -0.1486];
Beta = [-0.0342 , -0.001 , -0.0001 , -0.001, -0.001, -0.001];
disp('R30 Th 90')
a = Alpha(1);
b = Beta(1);
x = R30Th90X;
F_aMax = a * max(x.^3)
F_bMax = b * max(x)
figure;
subplot(2,1,1)
title('R30 Th 90')
hold on
plot(x,a*(x.^3),'*')
plot(x,b*x, '*')
plot(x,(a*(x.^3) + b*x))
legend 'ax^3' 'bx' 'R30Th90'
grid on;
hold off
subplot(2,1,2)
hold on
plot(x,(a*(x.^3) + b*x)/max(a*(x.^3) + b*x))
legend 'Normalized Torque'
```

```
54. grid on;
55. disp('R30 Th 120')
56. a = Alpha(2);
57. b = Beta(2);
58. x = R30Th120X;
59. F_aMax = a * max(x.^3)
60. F_bMax = b * max(x)
61. figure;
62. subplot(2,1,1)
63. title('R30 Th 120')
64. hold on
65. plot(x,a*(x.^3),'*')
66. plot(x,b*(x), '*')
67. plot(x,(a*(x.^3) + b*x))
68. legend 'ax^3' 'bx' 'Torque'
69. grid on;
70. hold off
71. subplot(2,1,2)
72. plot(x,(a*(x.^3) + b*x)/max(a*(x.^3) + b*x))
73. legend 'Normalized Torque'
74. grid on;
75. disp('R45 Th 90')
76. a = Alpha(3);
77. b = Beta(3);
78. x = R45Th90X;
79. F_aMax = a * max(x.^3)
80. F_bMax = b * max(x)
81. figure;
82. subplot(2,1,1)
83. title('R45 Th 90')
84. hold on
85. plot(x,a*(x.^3),'*')
86. plot(x,b*(x), '*')
87. plot(x,(a*(x.^3) + b*x))
88. legend 'ax^3' 'bx' 'Torque'
89. grid on;
90. hold off
91. subplot(2,1,2)
92. hold on
93. plot(x,(a*(x.^3) + b*x)/max(a*(x.^3) + b*x))
94. legend 'Normalized Torque'
95. grid on;
96. disp('R45 Th 120')
97. a = Alpha(4);
98. b = Beta(4);
99. x = R45Th120X;
```

```
F_aMax = a * max(x.^3)
F_bMax = b * max(x)
figure;
subplot(2,1,1)
title('R45 Th 120')
hold on
plot(x,a*(x.^3),'*')
plot(x,b*(x), '*')
plot(x,(a*(x.^3) + b*x))
legend 'ax^3' 'bx' 'Torque'
grid on;
hold off
subplot(2,1,2)
plot(x,(a*(x.^3) + b*x)/max(a*(x.^3) + b*x))
legend 'Normalized Torque'
grid on;
disp('R60 Th 90')
a = Alpha(5);
b = Beta(5);
x = R60Th90X;
F_aMax = a * max(x.^3)
F_bMax = b * max(x)
figure;
subplot(2,1,1)
title('R60 Th 90')
hold on
plot(x,a*(x.^3),'*')
plot(x,b*(x), '*')
plot(x,(a*(x.^3) + b*x))
legend 'ax^3' 'bx' 'Torque'
grid on;
hold off
subplot(2,1,2)
plot(x,(a*(x.^3) + b*x)/max(a*(x.^3) + b*x))
legend 'Normalized Torque'
grid on;
disp('R60 Th 120')
a = Alpha(6);
b = Beta(6);
x = R60Th120X;
F_aMax = a * max(x.^3)
F_bMax = b * max(x)
figure;
subplot(2,1,1)
title('R60 Th 120')
hold on
```

```
plot(x,a*(x.^3),'*')
plot(x,b*(x) , '*')
plot(x,(a*(x.^3) + b*x))
legend 'ax^3' 'bx' 'Torque'
grid on;
hold off
subplot(2,1,2)
plot(x,(a*(x.^3) + b*x)/max(a*(x.^3) + b*x))
legend 'Normalized Torque'
grid on;
```

d) Script for comparing the 7th and 3rd degree fitting to the FVS.

```
clc
clear
load("dThetaTime.mat")

theta_0 = 0;
time_0 = time2(104);
time_f = time2(end);
theta_dot_0 = dtheta2(104);
k_l_exp = 0.001;
k_nl_exp = 1.0682;
k_l_simulated = 0.001;
k_nl_simulated = 1.2701;


Ix = 11.599*10^(-6);
c = 0.00001;
t_span = [time_0:0.002:time_f];
InitialCond = [theta_0,theta_dot_0];
k7_7 = 14.904;
k7_5 = -3.0257;
k7_3 = 0.4762;
k7_1 = 0.0633;

[t_1,theta_1]                    =                    ode45(@(t1,theta_1)
   theta_system7(t1,theta_1,Ix,c,k7_1,k7_3,k7_5,k7_7),t_span,InitialCond);
[t_2,theta_2]                    =                    ode45(@(t2,theta_2)
   theta_system(t2,theta_2,Ix,c,k_l_exp,k_nl_exp),t_span,InitialCond);

figure;
hold on;
plot(t_1, theta_1(:,2),'o');
plot(time2(104:end),dtheta2(104:end),'red')
plot(t_2,theta_2(:,2),'+')
xlabel('Time (s)');
ylabel('$\dot{\theta}$ (rad/s)','Interpreter', 'latex');
legend '7th-Degree-Fitting' 'experimental' '3rd-Degree-Fitting'
grid on;
```

```
hold off;
function dthdt = theta_system7(t,theta,Ix,c,k_1,k_3,k_5,k_7)

    Fc=12;
    Fbrk=Fc+5;
    vbrk=15;
    vst=sqrt(2)*vbrk;
    vC=vbrk/10;
    dthdt = zeros(2,1);
    dthdt(1) = theta(2);
    %dthdt(2) = -27*tanh(theta(2)/3) -(c/Ix)*theta(2) - (k_l/Ix)*theta(1) -
(k_nl/Ix)*theta(1)^5;
    dthdt(2)                =                -sqrt(2*exp(1))*(Fbrk-Fc)*exp(-
(theta(2)/(vst))^2)*(theta(2)/vst)-Fc*tanh(theta(2)/vC)-(c/Ix)*theta(2)    -
(k_7*theta(1)^7 - k_5*theta(1)^5  + k_3*theta(1)^3 + k_1*theta(1))/Ix;
end
function dthdt = theta_system(t,theta,Ix,c,k_l,k_nl)

    Fc=9;
    Fbrk=Fc+5;
    vbrk=15;
    vst=sqrt(2)*vbrk;
    vC=vbrk/10;
    dthdt = zeros(2,1);
    dthdt(1) = theta(2);
    %dthdt(2) = -27*tanh(theta(2)/3) -(c/Ix)*theta(2) - (k_l/Ix)*theta(1) -
(k_nl/Ix)*theta(1)^5;
    dthdt(2)                =                -sqrt(2*exp(1))*(Fbrk-Fc)*exp(-
(theta(2)/(vst))^2)*(theta(2)/vst)-Fc*tanh(theta(2)/vC)-(c/Ix)*theta(2)    -
(k_nl*theta(1)^3 + k_l*theta(1))/Ix;
end
```